Eur. J. Mineral.
2016, **28**, 513–536
Published online 5 May 2016

Paper presented at the
8th European Conference on Mineralogy and Spectroscopy,
Rome, September 9–11, 2015

Short-range atomic arrangements in minerals. I: The minerals of the amphibole, tourmaline and pyroxene supergroups

FRANK C. HAWTHORNE*

Department of Geological Sciences, University of Manitoba, Winnipeg, Manitoba, Canada R3T 2N2
*Corresponding author, e-mail: frank_hawthorne@umanitoba.ca

Abstract: Spectroscopy is a key aspect of deriving local arrangements of atoms in minerals. Vibrational spectroscopy in the principal O–H-stretching region and MAS NMR spectroscopy are sensitive to such local arrangements, and play a crucial role in characterizing local structure in minerals in which there is solid solution. Variation in local arrangements of ions around a "probe" ion such as $(OH)^-$ can produce shifts in the energy of the principal O–H-stretching frequency, providing a window into those local arrangements. Similarly, variation in local arrangements around a "probe" isotope such as ^{27}Al or ^{29}Si can produce shifts in resonance energy that are indicative of differences in local environment. It is useful to develop a *configuration symbol* for the structural environment of the probe species, *i.e.*, the configuration of nearest-neighbour and next-nearest-neighbour polyhedra/sites, and then the local *arrangements* of atoms may be expressed in terms of this configuration symbol. Work on the monoclinic *C*2/*m* amphiboles, tourmaline and monoclinic pyroxene is reviewed here in terms of the particular effects that can give rise to absorptions in the principal O–H-stretching region of vibrational spectra. It is notable that the nearest-neighbour configurations in the amphibole, tourmaline and mica structures are topologically identical, and hence there should be strong spectral characteristics that are common to minerals of all three structure types. The spectra of the *C*2/*m* amphiboles show strong next-nearest-neighbour effects, and one expects such effects to occur also in spectra of minerals of the tourmaline (and mica) supergroups. The valence-sum rule of local bond-valence theory provides a strong constraint on possible local arrangements involved in heterovalent solid-solution in these minerals.

Key-words: short-range arrangement; long-range order; infrared spectroscopy; Raman spectroscopy; MAS NMR spectroscopy; amphibole; tourmaline; pyroxene; local bond-valence theory.

1. Introduction

In the past 50 years, there has been an enormous amount of work on long-range order-disorder (LR-OD) of atoms in minerals. This has been accompanied by investigations into the relations between mineral composition, structural state, physical properties and ambient conditions of crystallization or equilibration. The experimental techniques by which this work is done have seen considerable development over this time, and both diffraction and spectroscopic methods are now capable of producing results of high precision and considerable accuracy. However, LR-OD is only one type of atomic-scale order that occurs in minerals; there are also [1] short-range order-disorder (SR-OD), and [2] nanoscale order-disorder (N-OD), Here, I will focus on SR-OD, although N-OD is also of great importance, particularly with respect to (i) mechanisms of exsolution, and (ii) measuring spectroscopic properties of minerals.

The problem is that SR-OD does not obey the translational symmetry of the structure in which it occurs, and hence SR-OD is difficult to detect and decipher directly by standard diffraction methods. However, this does not mean that we can ignore it; as we shall see here, SR-OD is an important characteristic of many rock-forming and rare accessory minerals. There is information on SR-OD resident in diffuse scattering from a crystal (*e.g.*, Keen & Goodwin, 2015), but this information is quite difficult to extract, particularly when the SRO is complicated, and this approach has only been used for (mineralogically) simpler materials. SRO can be detected by several spectroscopic techniques [*e.g.*, vibrational spectroscopy, magic-angle-spinning nuclear magnetic resonance (MAS NMR) spectroscopy], but the problem here is that only part of the local arrangement is derived, and the complete picture of SR-OD is often not clear. Moreover, the sample requirements of such techniques can be rather severe in terms of what Nature provides for us to work with. Here, I shall examine SR-OD of cations and anions in a variety of minerals, review some of the experimental results, and show that detailed information on SR-OD can often be derived by *local* bond-valence theory. Why should we be interested in SR-OD? We should be interested in SR-OD because it will affect the stability of a mineral in the same way as LR-OD: through its associated configurational entropy and enthalpy of order-disorder. It will also affect the exchange of elements between coexisting minerals, and it can be a major

DOI: 10.1127/ejm/2016/0028-2538
0935-1221/16/0028-2538 $ 10.80

factor in controlling the possible variation in chemical composition of minerals, particularly those where heterovalent substitutions are extensive. Using formal valences for each ion, *e.g.*, Mg^{2+}, greatly complicates the expression of local atomic arrangements involving long strings of ions, and hence I will omit the formal valence of an ion except (1) where ions of the same element can exist in different valence states in the geological environment, and (2) for O^{2-} where oxygen is not associated with H as an (OH) group.

2. Long-range order-disorder

Let us examine the issue of LR-OD for a simple (two-dimensional) crystal for the case where there are two distinct sites, *M*(1) and *M*(2), in the unit cell (Fig. 1a), and let the general composition of the crystal be M_2SiO_4, where $M = Mg^{2+}$, Fe^{2+}. If the structure has perfect translational symmetry, every unit-cell is identical and all *M*(1) sites are occupied by the same type of cation; likewise, the *M*(2) sites are also occupied by the same type of cation, although not necessarily the same type of cation as is at *M*(1). This structure shows perfect long-range (and short-range) order, and must have the bulk chemical compositions Mg_2SiO_4 (where $M(1) = Mg_{1.0}$ and $M(2) = Mg_{1.0}$), $MgFe^{2+}SiO_4$ (where $M(1) = Mg_{1.0}$ and $M(2) = Fe^{2+}{}_{1.0}$, or $M(1) = Fe^{2+}{}_{1.0}$ and $M(2) = Mg_{1.0}$), or $Fe^{2+}{}_2SiO_4$ (where $M(1) = Fe^{2+}{}_{1.0}$ and $M(2) = Fe^{2+}{}_{1.0}$).

For compositions where $Mg \neq Fe^{2+}$, $Mg > 0.0$ and $Fe^{2+} > 0.0$, it is apparent that there can no longer be perfect translational symmetry, which is congruent with perfect long-range order: some *M*(1) sites must be occupied by Mg and some *M*(1) sites must be occupied by Fe^{2+}, or some *M*(2) sites must be occupied by Mg and some *M*(2) sites must be occupied by Fe^{2+}, or both. Thus such compositions must show some long-range disorder. Consider a (two-dimensional) crystal of composition $Mg_x\ Fe^{2+}{}_{(2-x)}\ SiO_4$ ($0 < x < 1$ or $1 < x < 2$). There cannot be perfect translational symmetry as the stoichiometry of the chemical composition does not match the "stoichiometry" of the sites in the unit cell of the crystal structure. Maximum LRO involves complete occupancy of one site by one cation and occupancy of the other site by a mixture of cations: either *M*(1) or
M(2) can be fully occupied by Fe^{2+} (or Mg), leading to four possible LRO arrangements. Long-range disorder occurs when Mg and Fe^{2+} occur in equal amounts at the *M*(1) and *M*(2) sites. The states of long-range order can be determined by various diffraction and spectroscopic techniques (*e.g.*, Hawthorne, 1983a and b), and there has been much work in the characterization of long-range order in the minerals discussed here: amphibole: *e.g.*, Hawthorne & Oberti (2007), Oberti *et al*. (2007); tourmaline, *e.g.*, Bosi (2011), Bosi & Lucchesi (2004); pyroxene, *e.g.*, Cameron & Papike (1980). Why are we interested in such states of LRO? We are interested because the state of LRO affects the stability of the crystal through the associated configurational entropy and enthalpy of order-disorder, and calibration of LRO as a function of temperature and pressure can lead to the development of geothermobarometers.

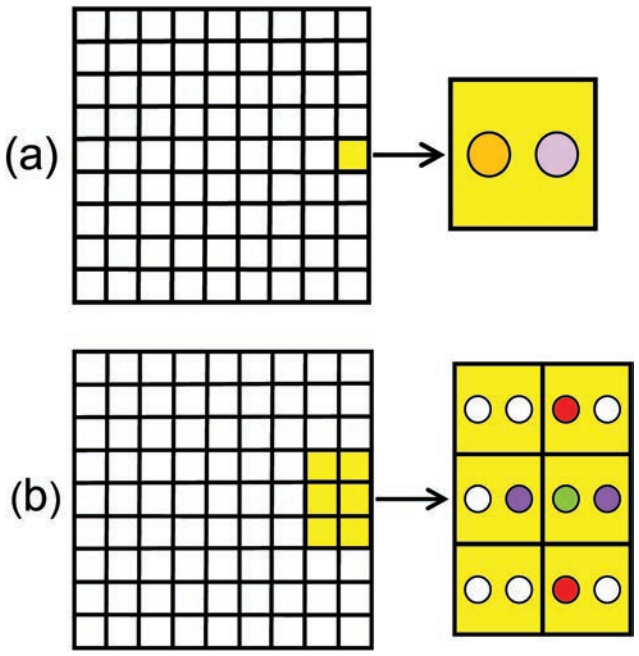

Fig. 1. A cartoon of a two-dimensional crystal structure (a) with two cation sites, *M*(1) (orange) and *M*(2) (mauve), in each unit cell, and (b) showing different occupancies of the sites in different unit cells (indicated by coloured circles).

3. Short-range order

Let us now consider SR-OD for the same (two-dimensional) structure (Fig. 1b). Long-range order-disorder involves the occupancies of the sites *averaged over the complete crystal*, whereas SR-OD involves the occupancies of individual (*i.e.*, non-averaged) sites over a scale of a few Å. In Figure 2, the *M*(1) site in the central unit cell is surrounded by four other sites, two *M*(1) sites and two *M*(2) sites: SR-OD involves the formation of *local* clusters of atoms that occur more, equal to, or less than that predicted by a random distribution. The four nearest-neighbour (NN) *M* sites surrounding the central *M*(1) site [Fig. 2: two *M*(1) and two *M*(2) sites] may be occupied by different clusters of cations (Fig. 2a and b).

3.1. Types of SR-OD

I will divide SR-OD into two broad types involving (1) homovalent ions, and (2) heterovalent ions. This division is made primarily because the atomic-scale mechanisms underlying the behaviour is dealt with in different ways.

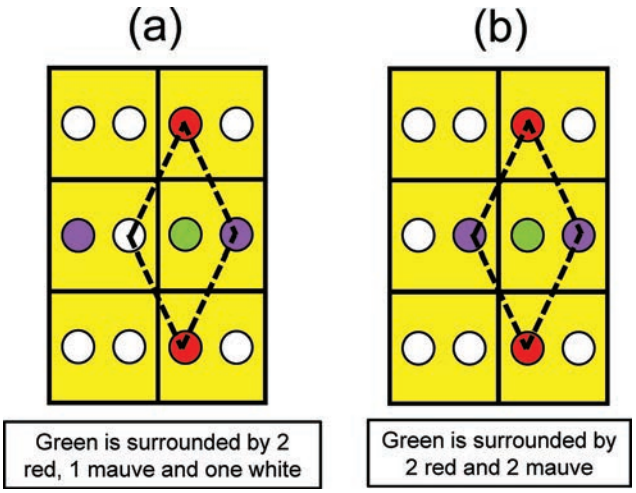

Fig. 2. A cartoon of short-range order in a two-dimensional crystal that shows six unit-cells (in yellow), each with two cation sites, *M*(1) and *M*(2). There may be various short-range arrangements of cations around a central *M*(1) site (green) involving (a) two red, one mauve and one white atoms, and (b) two red and two mauve atoms.

3.1.1. Homovalent ions

Many free ions are (approximately) spherical, and replacement of one by another in a structure should ideally cause an isotropic expansion of the atomic arrangement. In some structures, the high symmetry and isodesmic nature of the structure allows such behaviour [*e.g.*, (Na,K)Cl]. However, in most structures, non-cubic symmetry and the anisodesmic nature of the atomic arrangement can prevent the structure from responding to homovalent changes in composition in an isotropic fashion. Non-equivalent coordination polyhedra may not change in size in the same manner with changing occupancy, and the local structure will adjust accordingly [*e.g.*, $(Mg,Fe^{2+})SiO_3$ orthopyroxene].

As the local arrangements involved do not have large differences in the strengths of their chemical bonds (as is the case for disorder of heterovalent ions), the evaluation of these differences and their effects on local structure require more computationally intensive energetic methods. However, similar insight into the local features and their origin may be derived (*e.g.*, Bosenick *et al.*, 2000; Freeman *et al.*, 2006).

3.1.2. Heterovalent ions

Differences in the valence of an ion at a site can result in considerable changes in the strengths of the chemical bonds involved. Bond-valence theory (Brown, 2002, 2009) is a very useful way to consider the effect of these changes. Bond valence is a measure of the strength of a chemical bond. Brown & Shannon (1973) described a relation between bond valence and the length of a bond whereby for any given pair of bonded atoms, the bond valence is inversely proportional to bond length: higher bond-valences are associated with shorter bond-lengths. The ratios of the bond valences are thus related to the ratios of the associated bond-lengths. However, we need to scale these ratios in order to obtain specific values for the bond valences. This is done in the following manner: A bond valence is assigned to each bond such that *the sum of the bond valences at each atom is equal to the magnitude of the atomic valence*; this constraint is known as the *valence-sum rule*. Bond valences are scaled to the formal valences of the cations and anions involved in the chemical bonds. If the interatomic distances are known, bond valences can be calculated from the curves of Brown (2002) or Gagné & Hawthorne (2015). If the interatomic distances are not known, bond valences can be (1) approximated by Pauling bond strengths (Pauling, 1960), or (2) calculated by the method described by Brown (2002, Appendix 3). The valence-sum rule is a major constraint on a crystal structure: if an atomic arrangement proposed for a crystal does not (approximately) accord with the valence-sum rule, the structure is not correct. A major corollary of this statement is that if an atomic arrangement does not accord reasonably well with the valence-sum rule, it cannot be stable (*i.e.*, exist).

The valence-sum rule was derived to deal with crystal structures, *i.e.*, the long-range structure derived from conventional crystal-structure refinement of Bragg-diffraction data. Hawthorne (1997) proposed that bond-valence theory in general, and the valence-sum rule in particular, is also applicable to short-range atomic arrangements. The effect of this is illustrated in Figure 3. Figure 3a shows a local arrangement of atoms, with a central O anion bonded to one [4]-coordinated Si, two [6]-coordinated Mg and one [6]-coordinated Ca cations (the charge is omitted except where different valence states occur in geological environments). The bond valences are approximated by Pauling bond-strengths, and accord with the valence-sum rule as shown below the arrangement in Fig. 3a.

If we locally replace one Mg by Al and Ca by Li (Fig. 3b), the sum of the bond valences incident at the anion becomes $^{Si}1.0 + {}^{Mg}0.33 + {}^{Al}0.50 + {}^{Li}0.33 = 2.00$ *vu*, also in accord with the valence-sum rule. If we replace one Mg by Al and Ca by Li but these substitutions are not locally associated, the atom arrangements in Fig. 3c and d result, and the corresponding bond-valence arrangements deviate from the valence-sum rule. The atom arrangements in Fig. 3a and b are favoured over those in Fig. 3c and d. The constraint of electroneutrality requires charge compensation, *e.g.*, Li + Al → Mg + Ca. However, the local version of the valence-sum rule requires more: it requires that Li be locally associated with Al such that we have overall electroneutrality *and* local adherence to the valence-sum rule.

4. Experimental characterization of short-range order-disorder

Atom arrangements are generally derived by scattering methods in which phase differences in measured quantities are used to derive the relative positions of atoms in a

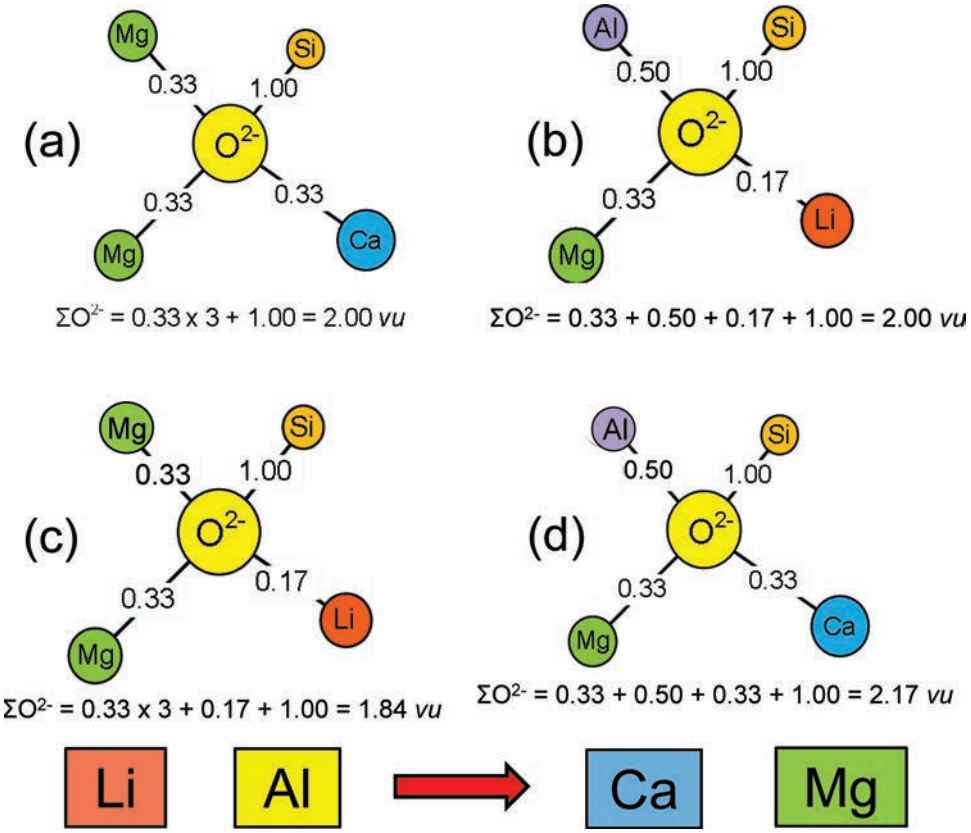

Fig. 3. Hypothetical clusters of cations around an O^{2-} anion (yellow); (a) a cluster of composition O-$^{[6]}Ca^{[6]}Mg_2^{[4]}Si$, with bond valences that show agreement with the valence-sum rule; (b) a cluster of composition O-$^{[6]}Li^{[6]}Al^{[6]}Mg^{[4]}Si$, again with bond valences that show agreement with the valence-sum rule; (c) a cluster of composition O-$^{[6]}Li^{[6]}Mg_2^{[4]}Si$, with bond valences that deviate from the valence-sum rule; (d) a cluster of composition O-$^{[6]}Ca^{[6]}Al^{[6]}Mg^{[4]}Si$, again with bond valences that deviate from the valence-sum rule.

structure. Well-ordered and moderately ordered crystal structures result in accurate atom identities and relative long-range positions. There is information on disorder and local structure in the diffuse (non-Bragg) scattering from a disordered crystal, but this information is not easy to extract as the weak scattering involved may not easily be distinguished from background noise, and where the disorder is complicated, the diffuse scattering may not contain sufficient resolved information to characterize the disorder, although more intense radiation sources and more sophisticated software (Keen & Goodwin, 2015) may improve this situation in the future.

Spectroscopic methods offer a different perspective on the issue of characterizing short-range order-disorder in atomic arrangements. Some spectroscopic methods are element- or ion-specific, and hence the behaviour of these elements/ions are not obscured by the other constituents of the material. Other spectroscopic methods energetically separate the effects of one or more elements/ions from the remaining constituents of the material, and again the behaviour of these elements/ions are not obscured by the other constituents of the material. Of course, the spectroscopic signals need to be calibrated against signals from crystallographically well-characterized material, but they offer insights into atomic arrangements that may not be derived by other methods.

There are many spectroscopic methods that may be used for this purpose, and most of these have been reviewed by Hawthorne (1988) and Henderson *et al.* (2014). Here I shall focus on two of the more common of these techniques: vibrational spectroscopy in the principal O–H-stretching region, and MAS NMR (Magic-Angle-Spinning Nuclear Magnetic Resonance) spectroscopy. There are obvious limitations to each of these methods: vibrational spectroscopy in the principal O–H-stretching region is limited to materials which contain hydrogen, and the H atoms must occupy only a small number of crystallographic sites; MAS NMR is not sensitive to all elements (isotopes) of interest, and until recently was not applicable to materials containing paramagnetic ions.

4.1. Vibrational spectroscopy in the principal O–H-stretching region

Reviews of experimental techniques and theoretical underpinnings of infrared and Raman spectroscopy plus applications are given by MacMillan & Hofmeister

(1988); McMillan & Hess (1988); Neuville *et al*. (2014) and Della Ventura *et al*. (2014a); Hawthorne & Waychunas (1988) discuss details of spectrum fitting. I will assume your familiarity with these topics and focus on issues that pertain specifically to the derivation of local atom arrangements. The number, positions and relative intensities of bands in the principal O–H-stretching region provide us with information concerning SR-OD, provided we can resolve the spectrum into its component bands. In turn, this depends on the positions and widths of the bands, and here I shall examine some issues pertinent to spectrum resolution.

4.1.1. Peak width and band width

The word "peak" is used to designate an envelope in the spectrum with only one maximum. The word "band" is used to indicate an absorption arising from a single local arrangement of atoms. Peak widths vary widely in the vibrational spectra of minerals, from a few wavenumbers to more than 100 wavenumbers. Many minerals show extremely broad peaks without obvious resolution of any component bands (*i.e*., without a change in the second derivative of the intensity with respect to energy, apart from those required to define the primary peak). There are (at least) three main reasons for broad peaks: (1) The peak may consist of more than one band, where the bands are not sufficiently resolved to produce changes in sign of the second derivative of wavelength with respect to energy; (2) Bands that are close in energy and physically close in the structure may couple to produce broadening. The infrared spectra of synthetic tremolite and synthetic richterite are shown in Fig. 4. In the spectrum of synthetic tremolite, the principal peak at 3674 cm^{-1} (which is also a single band) has a halfwidth of ~2 cm^{-1} (Fig. 4a), whereas in synthetic richterite, the principal peak at 3730 cm^{-1} has a halfwidth of ~25 cm^{-1} (Fig. 4b). End-member tremolite is completely ordered whereas end-member richterite is not; in richterite, the B component of the chemical formula is CaNa, and the local *M*(4) sites may each be occupied by Ca or by Na. There are two next-next-nearest neighbours to the $(OH)^-$ group in the monoclinic amphibole structure *M*(4)*M*(4) which, when combined with the composition, results in the following possible arrangements, *M*(4)*M*(4): CaCa, CaNa and NaNa; the intense 3730 cm^{-1} peak in the spectrum of synthetic richterite (Fig. 4b) must consist of three bands. As the intrinsic width of the CaCa (*i.e*., tremolite-type) band is ~2 cm^{-1}, assuming the same intrinsic width for the other two arrangements, the three bands cannot overlap to produce a composite peak ~25 cm^{-1} wide. The arrangements across the occupied *A* site couple to produce broadening of the component bands, and it is this coupling that produces the broad peak in the richterite spectrum (Fig. 4b). This coupling across occupied *A*-sites results in much broader peaks; such peaks occur in the spectra of *A*-site-filled amphiboles, and significantly hinder spectrum fitting.

In *A*-site-vacant amphiboles, the narrow line-width allows much more spectrum resolution and the recognition of more subtle features that are obscured by peak broadening in *A*-site-occupied amphiboles. The infrared spectrum of synthetic tremolite of nominal end-member composition (Fig. 4a) shows a shoulder to lower wavenumbers that was assigned to Mg occurring at the *M*(4) site. Gottschalk *et al*. (1999) showed that the intensity of this ~3669 cm^{-1} peak varies with the details of synthesis, and considered the possible local arrangements of Ca and Mg at the NNN *M*(4) sites using the configuration symbol *M*(1)*M*(1)*M*(3)–O(3)-*A*: *T*(1)*T*(1)–*M*(2)*M*(2)*M*(3)–*M*(1)*M*(1)*M*(2) *M*(2)***M*(4)*M*(4)*M*(4)*M*(4)** (in which the sites involved in the binary occupancy of *M*(4) by Ca and Mg are shown in bold). Table 1 shows the possible local arrangements of cations at this set of *M*(4) sites and their probabilities of occurrence for a random distribution. There are two distinct pairs of *M*(4) sites, and these are denoted in Table 1 as *nearer* and *further*. For a random distribution, bands G, H and I should have almost negligible intensity (≤0.02 %; Table 1) and bands D and E should be extremely weak (0.23 %; Table 1) due to the small amount of ^{B}Mg present in tremolite, leaving three

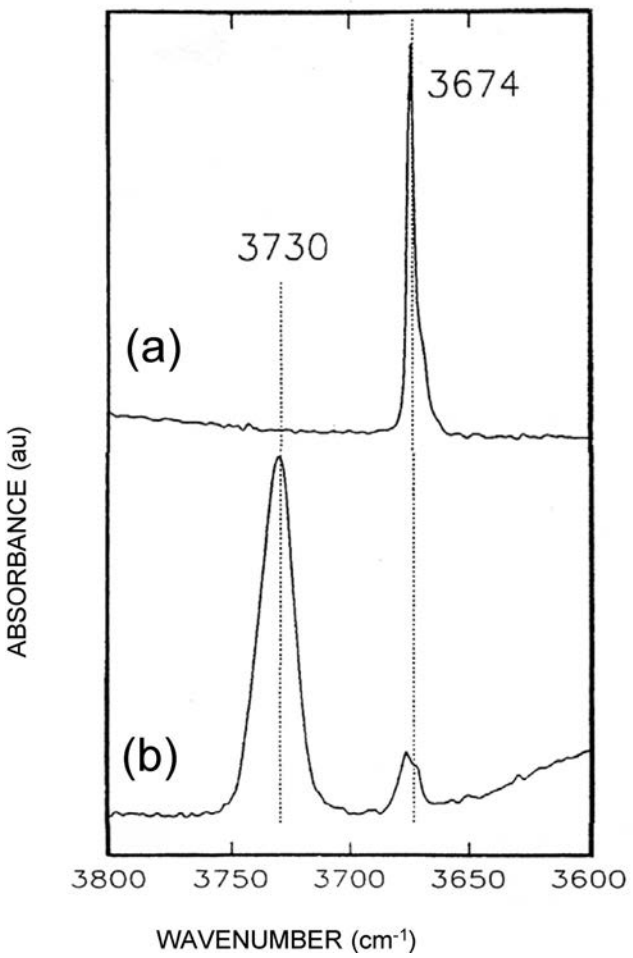

Fig. 4. Infrared absorption spectra in the principal O–H-stretching region for (a) synthetic tremolite, (b) synthetic richterite with a minor tremolite component. Modified from Hawthorne *et al*. (1996a).

Table 1. Probabilities for random distribution of Ca and Mg at $M(4)$ sites in the $C2/m$ amphibole structure; after Gottschalk *et al*. (1999).

	$M(4)M(4)$ nearer	$M(4)M(4)$ further	General probability	Probability for $x = 0.95$	$x = 0.05$
A	CaCa	CaCa	x^4_{Ca}	81.45	65.61
B	CaMg	CaCa	$2x_{Mg}x^3_{Ca}$	8.57	14.58
C	CaCa	CaMg	$2x_{Mg}x^3_{Ca}$	8.57	14.58
D	MgMg	CaCa	$x^2_{Mg}x^2_{Ca}$	0.23	0.81
E	CaCa	MgMg	$x^2_{Mg}x^2_{Ca}$	0.23	0.81
F	CaMg	CaMg	$4x^2_{Mg}x^2_{Ca}$	0.90	3.24
G	CaMg	MgMg	$2x^3_{Mg}x_{Ca}$	0.02	0.18
H	MgMg	CaMg	$2x^3_{Mg}x_{Ca}$	0.02	0.18
I	MgMg	MgMg	x^4_{Mg}	0.00	0.01

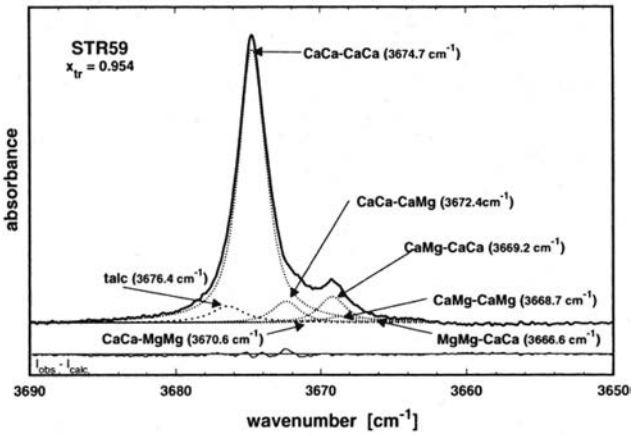

Fig. 5. Infrared absorption spectrum in the principal O–H-stretching region for synthetic tremolite, showing high-resolution of the fine structure to the lower-energy side of the spectrum and the corresponding band assignments. From Gottschalk *et al*. (1999).

arrangements of significant intensity. The spectrum of synthetic tremolite with close to the maximum observed content of ^{B}Mg has two distinct peaks (at 3674.7 and 3669.2 cm^{-1}; Fig. 5), but detailed fitting of the spectrum shows the presence of two additional peaks with significant intensity. The highest-energy band (3676.4 cm^{-1}) was assigned to minor talc in the run product (a common occurrence in amphibole synthesis, Raudsepp *et al*., 1991). The intense peak at 3674 cm^{-1} (Fig. 5) was assigned to $M(4)M(4)$–$M(4)M(4)$ = CaCa-CaCa, and the peaks at 3672.4 and 3669.2 cm^{-1} were assigned to CaCa-CaMg and CaMg-CaCa, respectively; some of the very weak bands were also assigned (Fig. 5). The relative peak intensities from the fitted spectrum of Fig. 5 are in accord with the probabilities of the arrangements calculated from a random distribution (Gottschalk *et al*., 1999), and thus $^{M(4)}$Ca and $^{M(4)}$Mg are short-range disordered in tremolite.

4.1.2. Variation in band intensity as a function of energy

Early work assumed that the relative intensities of bands in the principal O–H-stretching region are directly related to the relative amounts of the local arrangements of atoms related to these bands, implicitly assuming that the transition moment is the same for all local cation arrangements in the structure. Skogby & Rossman (1991) showed that the integrated molar absorptivity for the principal O–H-stretching-band in polarized single-crystal infrared absorption spectra of amphiboles increases with decreasing stretching frequency (Fig. 6a). The same effect was also observed by Groat *et al*. (1995) in polarized single-crystal spectra of vesuvianite, and Burns & Hawthorne (1994) showed this effect for

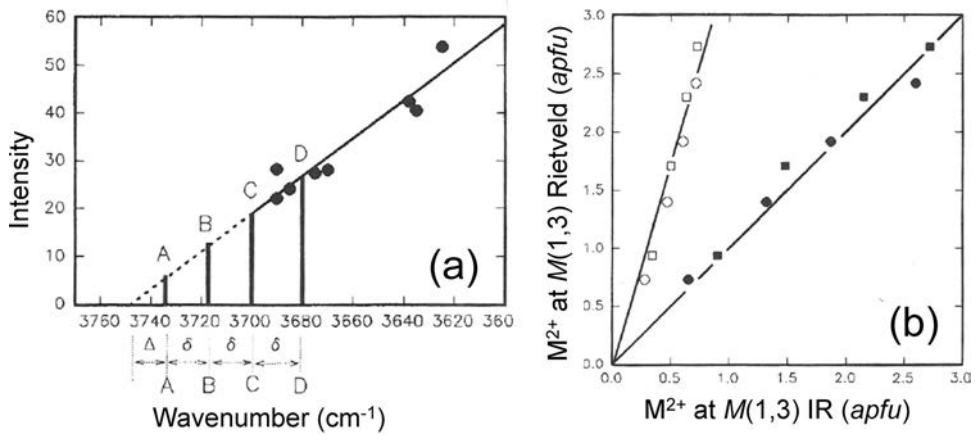

Fig. 6. (a) Variation in absorption intensity as a function of band energy, with the positions of the four bands in (Mg,Ni)-potassium-richterites and (Mg,Co)-potassium-richterites shown by the letters A, B, C and D; (b) variation in Co^{2+} content of the $M(1,3)$ sites in (Mg,Ni)-potassium-richterites and (Mg,Co)-potassium-richterites determined by Rietveld refinement and calculated from the intensities of the corresponding bands in the infrared using the relation of Skogby & Rossman (1991) (white circles) and assuming a 1:1 relation between band intensity and composition (black circles); (a) modified after Skogby & Rossman (1991), (b) modified after Della Ventura *et al*. (1996).

normalized O–H-stretching-band intensities in powder infrared spectra of borate minerals.

Della Ventura *et al*. (1996) synthesized two series of amphiboles: (Mg,Ni)-potassium-richterite and (Mg,Co)-potassium-richterite, and derived their site populations by Rietveld refinement. They also calculated the expected band intensities using the standard relation between site occupancies and probability of occurrence of local arrangements (assuming no SRO) (Hawthorne & Della Ventura, 2007, Appendix I) using two different models for the relation between molar absorptivity and absorption energy. Figure 6a shows the relation between peak intensity and energy derived by Skogby & Rossman (1991). The vertical lines at A, B, C and D in Fig. 6a show the positions of the four different arrangements of Mg and Ni/Co in these amphiboles, and the intensities of these peaks in the spectra can be combined with the relative intensities for the different energies of the A, B, C and D peaks to give the relation between the total Co and Ni at *M*(1,3) as determined by Rietveld refinement and as determined from the IR peak intensities and the molar absorptivity as a function of energy (hollow symbols in Fig. 6b). Also shown in Fig. 6b are the values calculated assuming that the molar absorptivity is constant with energy of absorption of the bands (solid symbols in Fig. 6b). It is apparent that the composition in these two amphibole series is determined correctly assuming that the molar absorptivity is constant with energy of absorption of the bands. Why is this the case? It is notable that the trends of the solid symbols in Fig. 6b depend on the relative intensities of the A,B,C,D bands. All the A,B,C,D arrangements occur in a single octahedral strip, and the absorptions will certainly couple to each other, perhaps negating any relative difference in transition probability. However, the absolute absorption may change (as a function of mean absorption energy, as measured by Skogby & Rossman, 1991) without affecting the relative absorption intensities.

4.2. Magic-Angle-Spinning Nuclear Magnetic Resonance spectroscopy

Reviews of experimental techniques and theoretical underpinnings of Magic-Angle-Spinning Nuclear Magnetic Resonance spectroscopy are given by Kirkpatrick (1988); Stebbins (1988) and Stebbins & Xue (2014). Again I will assume your familiarity with these topics and focus on issues that pertain specifically to the derivation of local atom arrangements.

Magic-Angle-Spinning Nuclear Magnetic Resonance (MAS NMR) spectroscopy is sensitive to specific isotopes, *e.g*., ^{29}Si, ^{27}Al, ^{6}Li. Consequently, it has the advantage that it can focus on the behaviour of specific nuclei, and the behaviour of these species is not confused by signals from the many other species that are insensitive to MAS NMR. There is no variation in band intensity specifically as a function of band energy, and hence the problems of variable molar absorptivity that plague infrared spectroscopy in the principle O–H-stretching region are not an issue in MAS NMR.

Until recently, a major problem of MAS NMR has been the fact that it could not be used for paramagnetic materials as the presence of paramagnetic species in a sample greatly affects peak widths and intensities, and induces very large shifts in frequency that are difficult to interpret. However, improvements in spinning speed and the introduction of new pulse sequences has led to the recent use of MAS NMR on paramagnetic materials (*e.g*., Wickramasinghe *et al*., 2008; Parthasarathy *et al*., 2013; Pell & Pintacuda, 2015). These developments will make a major difference to our understanding of short-range arrangements in minerals (*e.g*., Palke *et al*., 2015a and b), as many important rock-forming minerals involve solid-solutions of Fe^{2+} with other divalent cations.

5. Short-range order-disorder in amphiboles

Infrared spectroscopy in the principal O–H-stretching region of amphiboles has been used for over 50 years, initially to examine oxidation and dehydroxylation in Fe-bearing amphiboles (*e.g*., Addison & Sharp, 1962; Addison *et al*., 1962a and b; Clark & Freeman, 1967), then to characterize long-range order-disorder (*e.g*., Burns & Strens, 1966; Strens, 1966; Burns & Greaves, 1971), and more recently to examine short-range order-disorder (*e.g*., Robert *et al*., 1989, 1999; Della Ventura *et al*., 1996, 1998, 1999; Hawthorne *et al*., 1996a and b, 2000, 2005). It is particularly effective in recording different local arrangements of atoms around the (OH) group as the principal O–H-stretching frequency is particularly sensitive to differences in mass and charge of the ions coordinating the donor O atom, and to variations in the strength of the associated hydrogen bonding. There has been much less work using Raman spectroscopy, but recently Leissner *et al*. (2015) have shown that Raman spectroscopy is also very effective in understanding local arrangements in amphiboles.

The chemical formula of the amphiboles may be written very generally (Hawthorne & Oberti, 2007) as:

$$AB_2C_5T_8O_{22}W_2$$

where

A = Na, K, □, Ca, Li?;
B = Na, Li, Ca, Mn^{2+}, Fe^{2+}, Mg;
C = Mg, Fe^{2+}, Mn^{2+}, Al, Fe^{3+}, Mn^{3+}, Ti^{4+}, Li;
T = Si, Al, Ti^{4+};
W = (OH), F, Cl, O^{2-}.

A, B, C and T are groups of cations in this general formula that occupy the *A*, *M*(4), *M*(1,2,3) and *T* sites in the *C*2/*m* amphibole structure; note that the letters symbolizing the groups of ions are not italicized whereas the letters indicating the cation sites are italicized. With regard to the W anions, the O of the (OH) group and

the F, Cl and O^{2-} ions occupy the O(3) site and the H of the (OH) group occupies the H site, although it is usual to consider that the O(3) site is occupied by the (OH), F, Cl, O^{2-} ions (Hawthorne *et al*., 2012).

5.1. The O(3) site

In the *C*2/*m* amphibole structure, the O(3) site is occupied by (OH), F, Cl and O^{2-}, and commonly, (OH) is the dominant anion at O(3). The coordination of the O(3) site is illustrated in Fig. 7. The O(3) site is coordinated by two *M*(1) and one *M*(3) octahedra that share edges to form a triplet (Fig. 7a) with the H atom situated ~0.96 Å from the O(3) site (Hawthorne & Grundy, 1976). Figure 7b illustrates the two closest next-next-nearest neighbours to the O(3) site, sites that contain ions that interact directly with the H of the (OH) group. The H ion hydrogen bonds to the O(7) anion that bridges the nearest pair of *T*(1) tetrahedra (the broken line in Fig. 7b), and the cation at the *A* site has a repulsive interaction with the H ion. Figure 7c shows the remaining next-nearest-neighbours: (1) two *M*(2) and one *M*(3) octahedra each share two edges with octahedra of the nearest-neighbour *M*(1)*M*(1)*M*(3) trimer, and (2) two *M*(1) and two *M*(2) octahedra each share one edge with octahedra of the nearest-neighbour *M*(1)*M*(1)*M*(3) trimer.

5.2. Site-configuration symbol

In order to develop a systematic way of discussing the possible arrangements of atoms around the O(3) site in amphiboles, (Della Ventura *et al*., 1999) introduced a configuration symbol that describes the configuration of sites around the O(3) site:

$$M(1)M(1)M(3)\text{–}\mathrm{O}(3)\text{–}A : T(1)T(1)\text{–}M(2)M(2)M(3)$$
$$\text{–}M(1)M(1)M(2)M(2)$$

Local atomic arrangements may be expressed by substituting the relevant ions for the corresponding site symbols. Thus a common arrangement in pargasite is as follows: MgMgMg-(OH)-Na: SiAl-MgAlMg-MgMgMgMg.

5.3. Nearest-neighbour effects

In an amphibole with two cations occupying the *M*(1,2,3) sites, *e.g*., $K(CaNa)(Mg,Co)_5Si_8O_{22}(OH)_2$ or $\square(Fe,Mg)_2(Fe,Mg)_5Si_8O_{22}(OH)_2$, nearest-neighbour triplets *M*(1)*M*(1)*M*(3) may be occupied by MgMgMg, $MgMgM^{2+}$, $MgM^{2+}M^{2+}$ and $M^{2+}M^{2+}M^{2+}$, where M^{2+} = Co or Fe. As noted above, the principal O–H-stretching frequency is sensitive to the cations coordinating the donor O atom of the (OH) group. The infrared spectrum of synthetic $K(CaNa)(Mg_3Co_2)Si_8O_{22}(OH)_2$ (Fig. 8a) shows four bands that may be assigned to the local arrangements *M*(1)*M*(1)*M*(3) = MgMgMg, MgMgCo, MgCoCo and CoCoCo in order of decreasing wavenumber (energy). Similarly, the Raman spectrum of grunerite (Fig. 8b) shows four bands that may be assigned to the local arrangements *M*(1)*M*(1)*M*(3) = MgMgMg, $MgMgFe^{2+}$, $MgFe^{2+}Fe^{2+}$ and $Fe^{2+}Fe^{2+}$ Fe^{2+} in order of decreasing wavenumber.

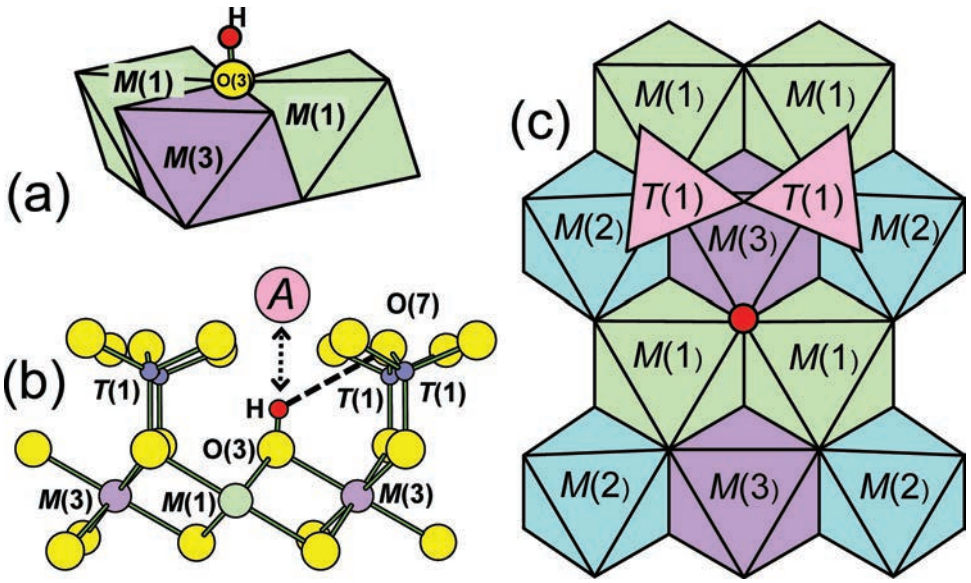

Fig. 7. The environment of the O(3) site in the *C*2/*m* amphibole structure; (a) perspective view showing the nearest-neighbour cluster of *M*(1)*M*(1)*M*(3) octahedra; (b) view down **b** showing the H...O(7) hydrogen bond and the repulsive interaction between an A cation and the H atom; (c) the nearest-neighbour and next-nearest-neighbour polyhedra around the H atom; yellow circles, O anions; red circle, H atom; pink circle, A-site; green circles, *M*(1) site; mauve circles, *M*(3) site; green octahedra, *M*(1); mauve octahedra, *M*(3) octahedra; the dashed black line is the H...O(7) hydrogen bond, the double arrow black line indicates a close approach of H and the *A*-site.

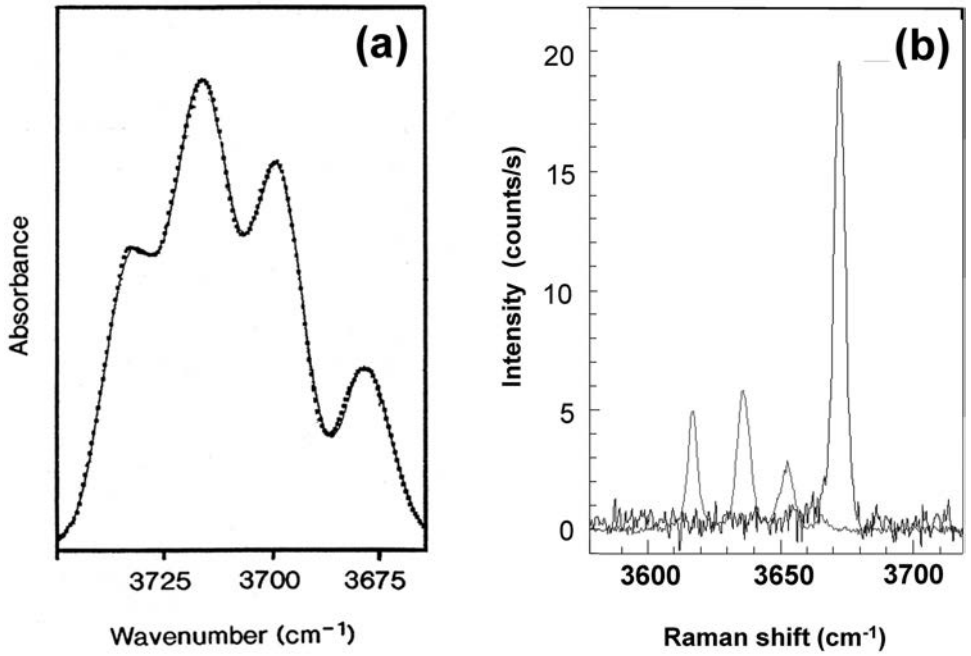

Fig. 8. Vibrational spectra in the principal O–H-stretching region: (a) infrared spectrum of $K(CaNa)(Mg_3Co_2)Si_8O_{22}(OH)_2$ from Hawthorne & Della Ventura (2007); (b) Raman spectrum of grunerite; modified from Leissner *et al*. (2015).

The widths of the bands in synthetic $K(CaNa)(Mg_3Co_2)Si_8O_{22}(OH)_2$ (Fig. 8a) are significantly larger than the widths of the corresponding bands in grunerite (Fig. 8b). This is not the result of the specific technique. In amphiboles with an occupied *A* site, coupling through the A cation broadens the bands due to local arrangements involving the configuration *M*(1)*M*(1)*M*(3)–O(3)–*A*; where the *A* site is vacant, this coupling does not occur and the bands are much narrower.

5.4. Next-nearest-neighbour effects

Figure 9 shows the infrared spectra of a synthetic tremolite of nominal end-member composition, a tremolite of composition $^{A}(K_{0.12}\ Na_{0.23})^{M(4)}(Ca_{1.81}\ Na_{0.15}\ Mg_{0.04})Mg_5\ ^{T}(Si_{7.79}\ Al_{0.21})O_{22}(OH_{0.67}F_{0.33})$ (labelled tremolite(56) by Hawthorne, 1983c), and two synthetic amphiboles with compositions along the join tremolite–richterite. The interesting feature of these amphiboles is that they all have the same (completely ordered) nearest-neighbour *M*(1)*M*(1)*M*(3) arrangement: MgMgMg as *C* = 5 Mg *apfu* (atoms per formula unit) in all these amphiboles. We must conclude from this that the differences in the spectra of Fig. 9 involve differences in next-nearest neighbours. From the chemical formula of tremolite(56), we see that the composition is dominated by the tremolite component, and the strongest peak in the spectrum in Fig. 9b is at 3674 cm^{-1}, as in synthetic tremolite (Fig. 9a). Tremolite(56) has significant richterite and edenite components, *i.e.*, richterite, $^{A}(K_{0.12}\ Na_{0.03})\ ^{M(4)}Na_{0.15}$; edenite, $^{A}Na_{0.20}\ ^{T}Al_{0.21}$. Inspection of Fig. 9c and d shows that richterite has its dominant peak at 3730 cm^{-1} whereas tremolite only has an extremely small absorption at this wavelength. Conversely, the local arrangement in edenite is MgMgMg–OH–Na:AlSi. Edenite is not well-characterized as it is extremely rare; however, the local arrangement of nearest- and next-nearest-neighbour cations around (OH) at O(3) in edenite is identical to that in pargasite, which is well-characterized (Della Ventura *et al*., 1999, 2014b). In pargasite, the local arrangement *M*(1)*M*(1)*M*(3)–O(3)–*A*: *T*(1)*T*(1) = MgMgMg–(OH)–Na:AlSi gives a band at 3705 cm^{-1} which corresponds to the second-strongest peak in tremolite(56) (Fig. 9b).

Why is the band due to the richterite constituent so weak relative to the amount of its content in the chemical formula of tremolite(56)? First, there is significant F at O(3) in tremolite(56); F has a strong tendency to prefer richterite compositions to tremolitic and pargasitic compositions (Della Ventura *et al*., 2001), and it seems likely that local richterite-like arrangements are preferentially associated with F at O(3) and hence invisible in the infrared. Thus we may conclude that the difference in the spectra of Fig. 9a and b is due to the presence of the next-nearest-neighbour arrangement *M*(1)*M*(1)*M*(3)–O(3)–*A*: *T*(1)*T*(1) = MgMgMg–(OH)–Na:AlSi (Fig. 10), indicating that next-nearest-neighbour effects are an important feature of amphibole infrared spectra, with the result that infrared spectroscopy can give us information on local arrangements beyond nearest neighbour in amphiboles.

Figure 11 shows the infrared spectra of a series of synthetic amphiboles of composition $NaCa_2(Mg_4M^{3+})$

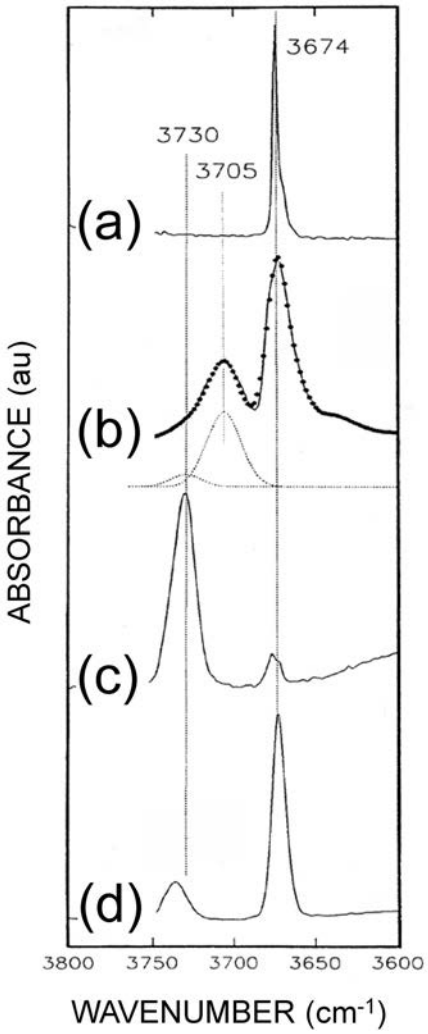

Fig. 9. Infrared spectrum in the principal O–H-stretching region of (a) synthetic tremolite; (b) tremolite(56) of Hawthorne & Grundy (1976); (c) synthetic richterite with minor tremolite component; (d) tremolite with a minor richterite component; after Hawthorne *et al*. (1996a).

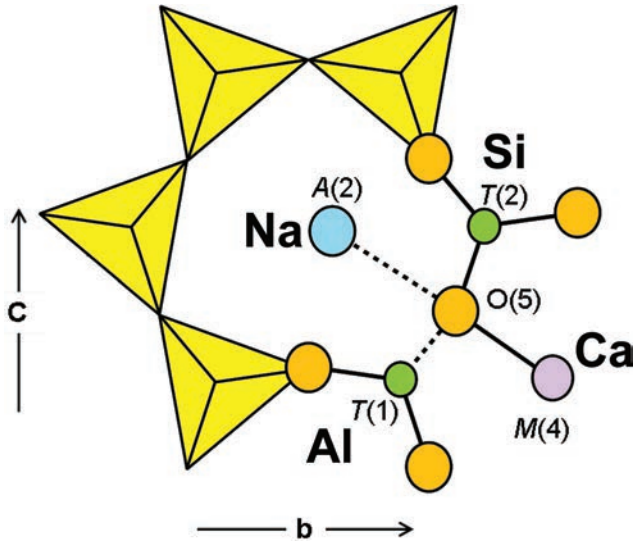

Fig. 10. The O(5) anion site in tremolite, together with the coordinating *A*(2), *M*(4), *T*(1) and *T*(2) sites.

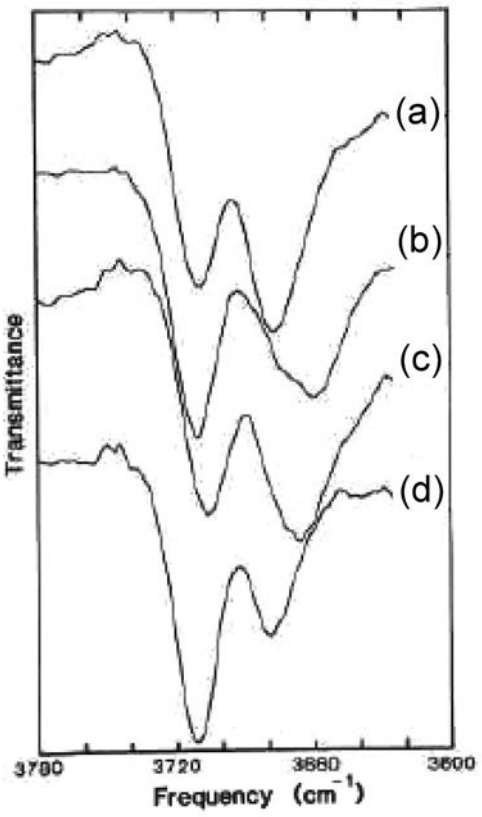

Fig. 11. Infrared spectrum in the principal O–H-stretching region of (a) synthetic pargasite; (b) synthetic Cr^{3+} pargasite; (c) synthetic Ga pargasite; (d) synthetic Sc pargasite. After Raudsepp *et al*. (1987).

$(Si_7Al)O_{22}(OH)_2$, where M^{3+} = Al, Cr^{3+}, Ga, Sc (Raudsepp *et al*., 1987), in which there are two broad envelopes at ~3715–3707 and ~3690–3670 cm^{-1}. In its ideally ordered state, $NaCa_2(Mg_4M^{3+})(Si_7Al)O_{22}(OH)_2$ would have the nearest-neighbour arrangement *M*(1)*M*(1) *M*(3)–OH = MgMgMg–OH. Inspection of Fig. 11 shows that this is not the case. The more intense envelope at ~3715 cm^{-1} may be assigned to the nearest-neighbour arrangement *M*(1)*M*(1)*M*(3)–OH = MgMgMg–OH. The other envelope must be due to the occurrence of M^{3+} at one (or more) of the NN sites [*i.e.*, M^{3+} is not completely ordered at the *M*(2) site]. Note that this assignment is in accord with that expected from bond-valence theory: the local presence of M^{3+} at the *M*(1,3) sites will increase the net bond-valence incident at the O(3) donor anion, leading to a weakening of the hydrogen bond to O(7) and a shift of the absorption to lower energy. This assignment was confirmed by crystal-structure refinement on both natural (*e.g.*, Oberti *et al*., 1995a; Tait *et al*., 2001; Heavysege *et al*., 2015) and synthetic amphiboles (Raudsepp *et al*., 1987,

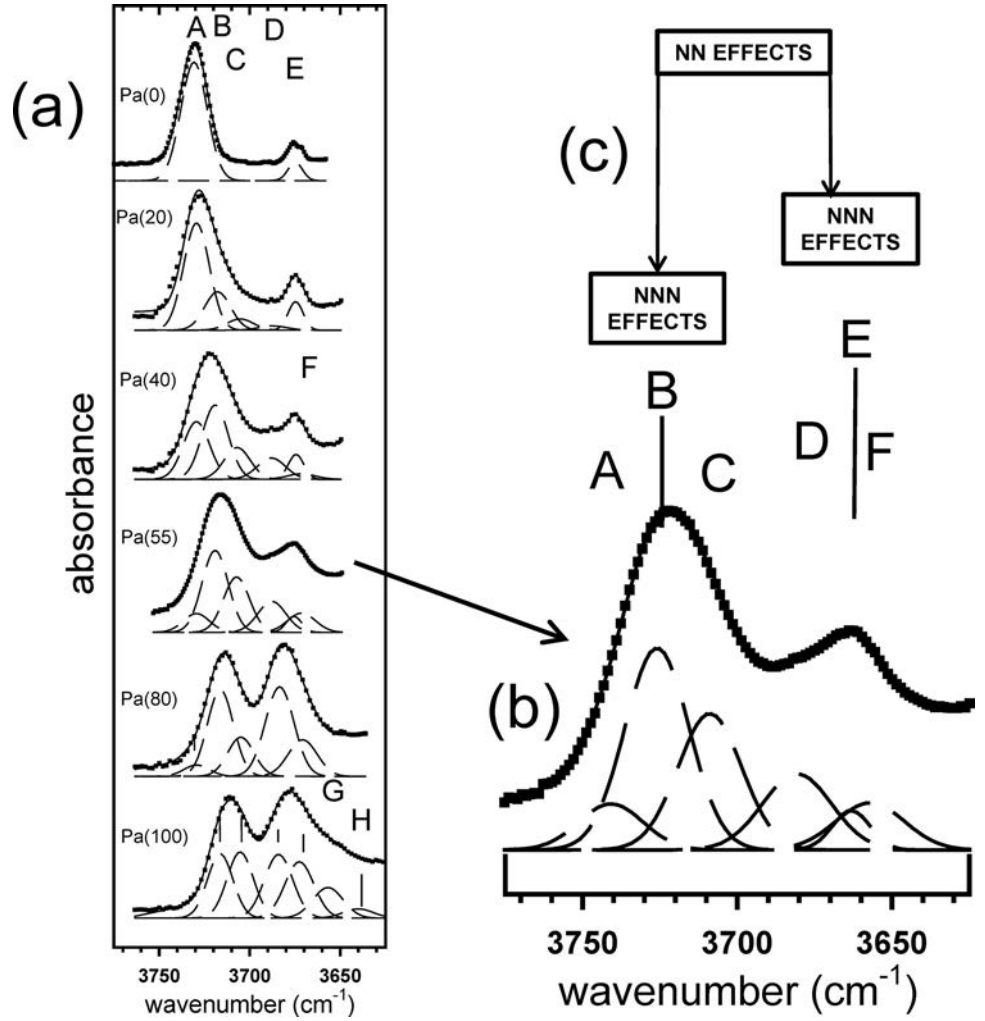

Fig. 12. (a) Infrared spectrum in the principal O–H-stretching region of (a) synthetic richterite–pargasite solid-solutions; (b) enlarged spectrum of Pa(55) spectrum; (c) showing the nearest-neighbour (NN) and next-nearest-neighbour (NNN) effects in the Pa(55) spectrum. After Della Ventura *et al*. (1999).

1991). However, note that this type of behaviour is perturbed by the presence of F, as crystal-structure refinement (*e.g*., Boschmann *et al*., 1994; Oberti *et al*., 1995b, 1998) shows that Al does not occur at *M*(1) and/or *M*(3) in synthetic fluoro-amphiboles.

Figure 12 shows the infrared spectra of synthetic amphiboles along the join richterite–pargasite: $Na(CaNa)Mg_5Si_8O_{22}(OH)_2$–$NaCa_2(Mg_4Al)(Si_7Al)O_{22}(OH)_2$ (Della Ventura *et al*., 1999). The spectra change radically from richterite to pargasite, and the six spectra can be fit collectively to a single model with eight bands (Fig. 12a, Table 2). The spectrum for $Pa_{55}Ri_{45}$ (Fig. 12b) shows a strong resemblance to the spectra of synthetic pargasite and substituted pargasites in Fig. 11: two broad envelopes at ~3720 and ~3662 cm^{-1}. As can be seen from Table 2, these broad envelopes are due to the nearest-neighbour arrangements *M*(1)*M*(1)*M*(3)–OH = MgMgMg–OH and MgMgAl–OH, respectively. However, within each envelope there is significant fine-structure. Note that although the fitting of this fine structure cannot be justified solely on the basis of the

Table 2. Possible cation arrangements around the OH group in synthetic amphiboles of the richterite-pargasite series, together with the assigned bands (A-H) and observed band frequencies in Pa(55); after Della Ventura *et al*. (1999).

	Local arrangement	Observed band frequency (cm^{-1})
A	[MgMgMg]–OH–^{A}Na: SiSi–MgMgMg–MgMgMgMg	3740
B	[MgMgMg]–OH–^{A}Na: SiAl–MgMgMg–MgMgMgMg	3723
C	[MgMgMg]–OH–^{A}Na: SiAl–MgMgAl–MgMgMgMg	3706
D	[MgMgAl]–OH–^{A}Na: SiAl–MgMgMg–MgMgMgMg	3680
E	[MgMgMg]–OH–$^{A}\square$: SiSi–MgMgMg–MgMgMgMg	3662
F	[MgMgAl]–OH–^{A}Na: SiAl–MgMgAl–MgMgMgMg	3655
G	[MgMgAl]–OH–^{A}Na: SiAl–MgMgAl–AlMgMgMg	—
H	[MgMgAl]–OH–^{A}Na: SiAl–MgMgAl–AlAlMgMg	—

spectrum shown in Fig. 12b, fitting of all eight spectra in the solid-solution series (together with the constraints imposed by their known bulk compositions) requires all eight bands listed in Table 2 for the complete series, and the model fitted to the spectrum in Fig. 12b is in accord both with its place in the solid solution and its bulk composition.

Examination of the bands in Fig. 12b and Table 2 shows that the fine structure in both envelopes involves the presence of variations in next-nearest-neighbour arrangements (Fig. 12c). Bands A, B and C show differences in next-nearest-neighbour A:$T(1)T(1)$ arrangements: Na: SiSi and Na: SiAl; and differences in next-nearest-neighbour $M(1)M(1)M(3)$ arrangements: MgMgMg and MgMgAl. Bands D, E and F show similar differences; next-nearest-neighbour A:$T(1)T(1)$ arrangements: Na: SiAl and □: SiSi; next-nearest-neighbour $M(1)M(1)M(3)$ arrangements: MgMgMg and MgMgAl.

5.5. Local coupling: one-mode and two-mode behaviour

5.5.1. One-mode behaviour

Figure 13a shows the infrared spectra of amphiboles of the fluoro-tremolite (upper) and tremolite (lower) series. There is a single peak in each spectrum; the change in composition does not produce an additional peak (note that the intensities do not scale with the (OH) content as the (powder) samples have different amounts of sample, and are affected differently by particle-scattering effects). This is known as *one-mode behaviour* (Chang & Mitra, 1968).

5.5.2. Two-mode behaviour

Figure 13b shows the infrared spectra of synthetic richterite (upper) and a synthetic F-richterite (lower). In both spectra, there is a weak peak at 3674 cm^{-1} corresponding to a small amount of tremolite component that is difficult to exclude from synthetic richterite. The important feature in the lower spectrum is the appearance of a second peak at 3711 cm^{-1} with substitution of some F into the richterite structure. This appearance of a second peak is known as *two-mode behaviour* (Chang & Mitra, 1968).

5.5.3. Local coupling

In synthetic tremolite–fluoro-tremolite solid-solutions, the one-mode behaviour (Fig. 13a) indicates that the (OH) group is not significantly affected by adjacent arrangements involving F, and we may conclude that there is no coupling between adjacent O(3) anions, either through the O(3)-O(3) edge in the octahedral strip or across the vacant A-site cavity. In synthetic richterite–fluoro-richterite solid-solutions, the two-mode behaviour (Fig. 13b) indicates

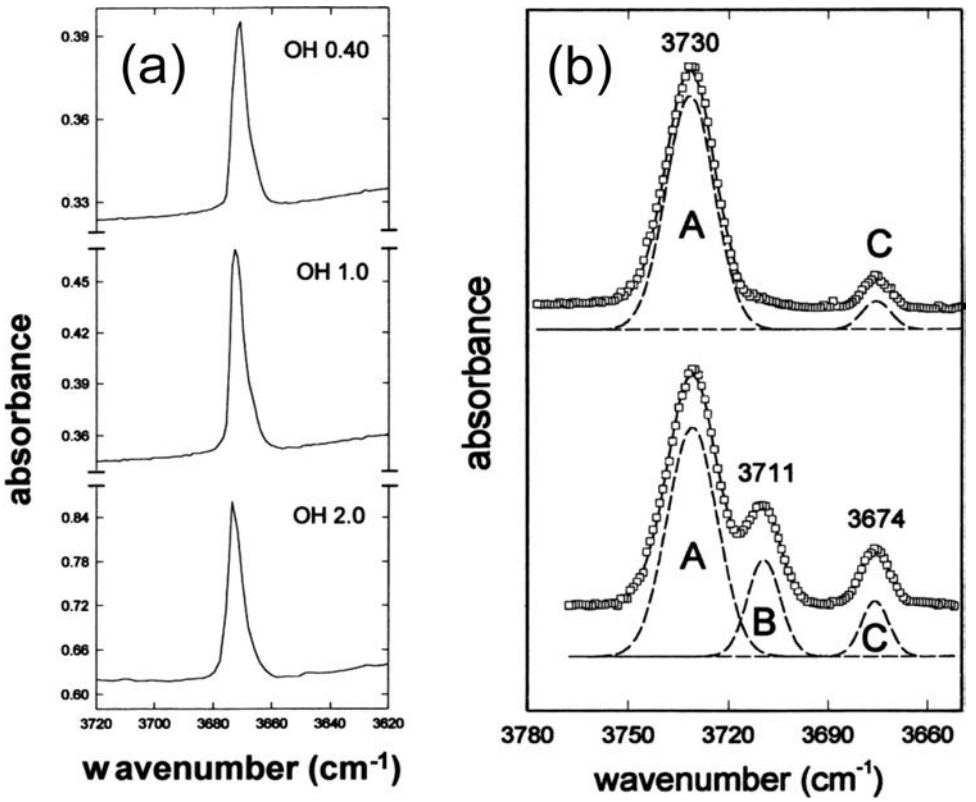

Fig. 13. Infrared spectrum in the principal O–H-stretching region of (a) tremolite–fluoro-tremolite solid-solutions, and (b) richterite–fluoro-richterite solid-solutions. After Robert *et al*. (1999).

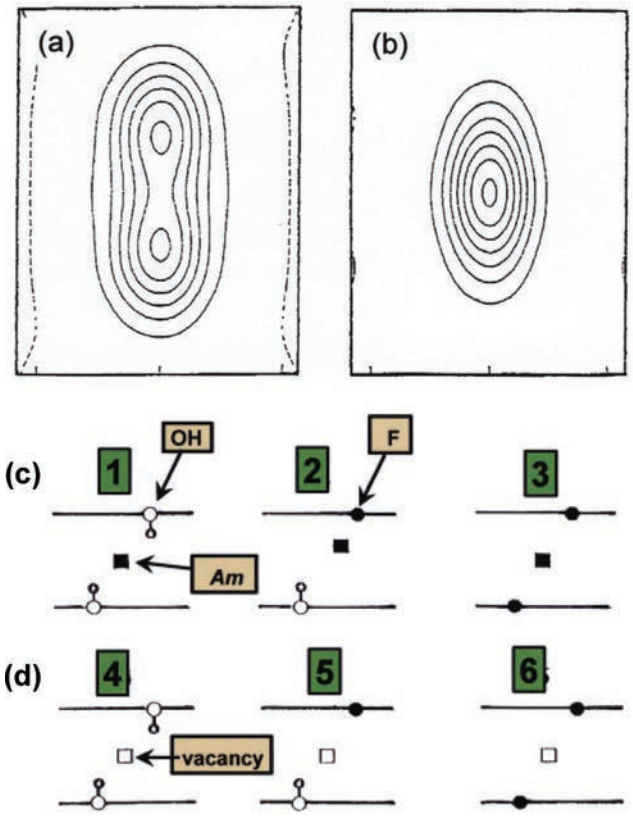

Fig. 14. (a,b) Electron-density distribution in the *A*-site cavity projected on to (-201) in (a) fluoro-arfvedsonite, and (b) arfvedsonite (contour interval is 1 e/Å^3); (c) local arrangements in the *A*-site cavity involving (OH) and F in (OH),F-bearing richterite and (OH),F-bearing tremolite: in richterite, the A cation is centered where locally O(3) = $(OH)_2$ or F_2 and is displaced away from (OH) where locally O(3) = (OH)F; in tremolite, there is no A-cation; (d) local arrangements in a vacant *A*-site cavity. Modified from Hawthorne & Della Ventura (2007).

that the (OH) group is significantly affected by adjacent arrangements involving F. In tremolite, the *A*-site is vacant, whereas in richterite the *A*-site is occupied by Na, suggesting that the two-mode behaviour in richterite is due to coupling of arrangements across the *A* cavity through the Na atom. The principal O–H-stretching frequencies in tremolite (3674 cm^{-1}) and richterite (3730 cm^{-1}) indicate that there is a strong repulsive interaction between H and Na at the *A*-site. Moreover, electron-density arrangements in the *A* cavity where O(3) = (OH) (Fig. 14a) and where O (3) = F (Fig. 14b) show that Na occupies a more central position in the cavity where O(3) = F than where O(3) = (OH) (Fig. 14c). Three local O(3)–*A*–O(3) arrangements are possible: (OH)–Na–(OH), (OH)–Na–F and F–Na–F. For the arrangement (OH)–Na–F, Na will be displaced toward F and away from (OH), reducing the repulsive interaction between H and Na and causing the (OH) group to absorb at a lower frequency than it will for the arrangement (OH)–Na–(OH), giving rise to an additional band in the spectrum of fluoro-richterite (Fig. 13b). Hence local coupling of (OH) occurs across an occupied *A* cavity but not across an unoccupied *A* cavity (Fig. 14d). This is an important generalization as it provides constraints on what bands can and cannot occur in such solid-solutions.

5.6. Previous work

The main focus of this paper is on the specific spectral characteristics that relate to the derivation of short-range atom arrangements, rather than on a comprehensive review of previous work. That said, Hawthorne & Della Ventura (2007) review all work to that date on the spectral characteristics of local arrangements in amphiboles.

6. Short-range order-disorder in tourmaline

The chemical formula of the tourmaline-supergroup minerals may be written very generally (Henry *et al*., 2011) as:

$$XY_3Z_6(T_6O_{18})(BO_3)_3V_3W$$

where

X = Na, Ca, K, and □ (vacancy);
Y = Fe^{2+}, Mg, Mn^{2+}, Al, Li, Fe^{3+}, Cr^{3+} and V^{3+};
Z = Al, Fe^{3+}, Mg, Fe^{2+}, Cr^{3+} and V^{3+};
T = Si, Al and B;
B = B;
V = (OH) and O^{2-};

W = OH, F and O^{2-}.

X, Y, Z, T and B are groups of cations that occupy the *X*, *Y*, *Z*, *T* and *B* sites in the *R*3*m* tourmaline structure; note that the letters symbolizing the groups of ions are not italicized whereas the letters indicating the cation sites are italicized. With regard to the V anions, O of the (OH) group and O^{2-} ions occupy the O(3) site; with regard to the W anions, the O of the (OH) group, F and O^{2-} ions occupy the O(1) site. The H ions occupy the H1 and H3 sites (Gatta *et al*., 2012, 2014).

6.1. The O(1) site

In the *R*3*m* tourmaline structure, the O(1) site is occupied by (OH), F and O, and commonly, (OH) is the dominant anion at O(3). The O(1) site (Fig. 15) is coordinated by three *Y* octahedra that share edges to form a triplet (Fig. 15a) with the H ion situated ~0.96 Å from the O(1) site (Gatta *et al*., 2012, 2014). The H(1) ion weakly hydrogen-bonds to the O (4) and O(5) anions (Gatta *et al*., 2014) (Fig. 15b and c), suggesting that substitution of Al for Si at the *T* site may shift the principal-stretching frequency for $^{O(1)}$(OH) to lower energies. The H(1)–*X* distance is ~2.36 Å, suggesting a very strong interaction between H(1) and any cation locally occupying the *X* site.

From a consideration of the relation between mean bond-length and constituent-cation radius, Hawthorne *et al*. (1993) showed that there is considerable disorder of Mg and Al over the *Y* and *Z* sites in tourmaline, and this conclusion was extended to Fe-bearing tourmalines by Bosi (2011) and Bosi & Lucchesi (2004); Taylor *et al*. (1995) used bond-valence arguments to show that where the O(1) site is occupied by O, the local arrangement of *Y* cations associated with $^{O(1)}O^{2-}$ is MgAlAl, which I will express here as $^{Y}Mg^{Y}Al^{Y}Al$–$^{O(1)}O^{2-}$. This idea was developed further by Hawthorne (1996) for local arrangements and their constraints on chemical composition in tourmalines. In elbaite, ideally $Na(Li_{1.5}Al_{1.5})Al_6(Si_6O_{18})(BO_3)_3(OH)_3(OH)$, the O(1) site has the combinatorially possible coordinations: $^{Y}Li^{Y}Li^{Y}Li$, $^{Y}Li^{Y}Li^{Y}Al$, $^{Y}Li^{Y}Al^{Y}Al$ and $^{Y}Al^{Y}Al^{Y}Al$; however, $^{Y}Li^{Y}Li^{Y}Li$ and $^{Y}Al^{Y}Al^{Y}Al$ are not possible with O(1) = (OH). Where O(1) = O, the arrangement $^{Y}Al^{Y}Al^{Y}Al$ is now feasible and $^{Y}Li^{Y}Li^{Y}Al$ is not feasible. The situation becomes much more flexible where elbaite can incorporate Mg, Fe^{2+} and/or Mn^{2+} at *Y* (*e.g*., Burns *et al*., 1994), and local arrangements involving mono-, di- and tri-valent cations are advantageous from a local bond-valence perspective. Hawthorne (1996) also showed that incorporation of ^{Y}Al and $^{O(1)}O$ is compatible with local bond-valence requirements around O(1) and suggested that substitution of Si by (Al,B) at *T* will be locally associated with R^{3+} at *Y* and possibly also with Ca at *X*. Hawthorne (2002) and Bosi & Lucchesi (2007) went on to examine the bond-valence and crystal-chemical constraints on compositional variation in the tourmaline structure.

In an important paper, Bosi (2013) carefully examined the local bond-valences incident at the O(1) site for *Y* = (Li,

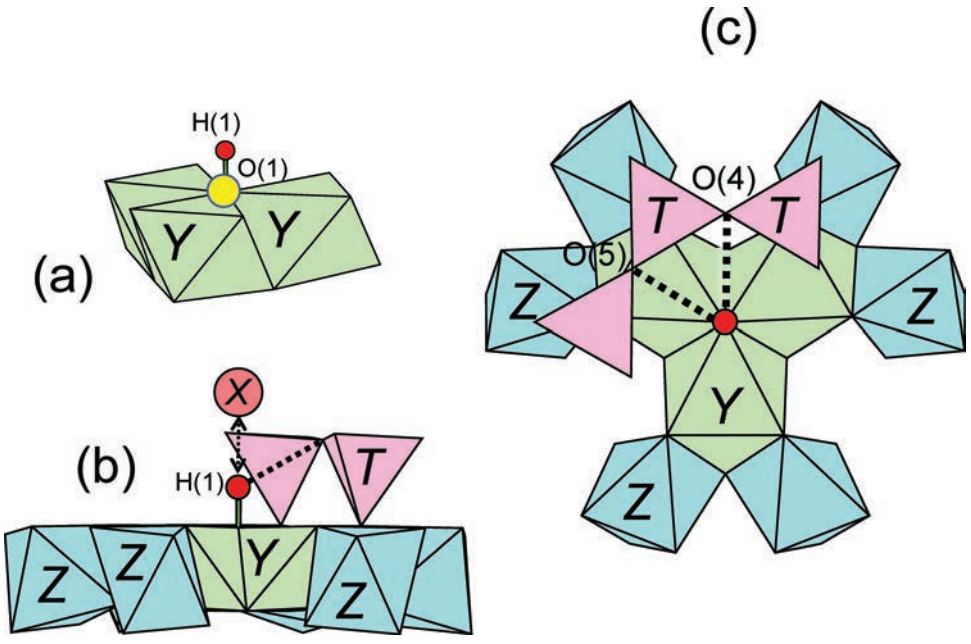

Fig. 15. The environment of the O(1) site in the tourmaline structure; (a) perspective view showing the nearest-neighbour cluster of *YYY* octahedra; (b) view down **b** showing the H(1)...O(4) hydrogen bond and the repulsive interaction between an X cation and the H(1) atom; (c) the nearest-neighbour and next-nearest-neighbour polyhedra around the H(1) atom; yellow circles: O anions; red circle: H(1) atom; pink circle: A-site; green octahedra: *Y*; pink tetrahedra: *T* tetrahedra; the dashed black lines are the hydrogen bonds involving H(1), the double arrow black line indicates a close approach of H(1) and the *X*-site.

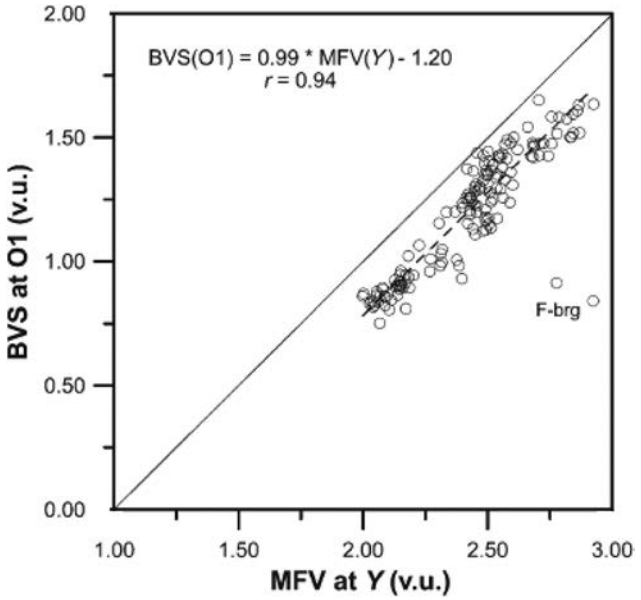

Fig. 16. Bond-Valence Sum incident at O(1) ($^{O(1)}$BVS) as a function of the Mean Formal Valence (MFV) at the *Y* site. The solid line is the ideal curve [$^{(O1)}$BVS = ^{Y}MFV(Y) – 1], passing through 1.0 and 2.0 at the O(1) anion for ^{Y}MFV = 2.0 and ^{Y}MFV = 3.0, respectively. Data for fluor-buergerite (F-brg) were not included in the linear fit (dashed line). From Bosi (2013).

R^{2+}, R^{3+}) and listed the allowed local arrangements of cations around F, (OH) and O^{2-} at the O(1) site. He then extended this approach by considering the bond valence incident at O(1) [BVS(O1)] as a function of the mean formal valence (MFV) of the cations occupying the *Y* site in a large number of refined structures. As shown in Fig. 16, there is a well-developed linear relation between these two variables. In an unstrained structure, the data should lie slightly above the 45° line as a result of the weak hydrogen-bonding of the H(1) ion, but the fact that the data lie below the line is in accord with extensive work by Bosi (2011) showing that there is significant structural strain in this region of the tourmaline structure. From Fig. 16 and following the arguments of Grice & Ercit (1993), Bosi (2013) derived the following equation for the estimation of the (OH) content of the O(1) site in *apfu*:

$$^{O(1)}(OH) = {}^{W}(OH) = 2 - \left[1.01 \times {}^{O(1)}\,BVS\right] - 0.21 - F$$

Table 3 lists the possible local charge arrangements around the O(1) site as indicated by adherence to the valence-sum rule, together with the corresponding cation-anion arrangements.

6.2. The O(3) site

The O(3) site is occupied by (OH) and O^{2-}, and (OH) is commonly the dominant anion at O(3). The coordination of O(3) is illustrated in Fig. 17. The O(3) site is coordinated by one *Y* and two *Z* sites that share edges to form a triplet of

Table 3. Charge arrangements in accord with the valence-sum rule at O(1), plus possible chemical arrangements.

Charge arrangement [*YYY*]-O(1)	Chemical clusters [*YYY*]-O(1)
$R^{2+}R^{2+}R^{2+}$–(OH),F	MgMgMg–(OH),F
	$MgMgFe^{2+}$–(OH),F
	$MgFe^{2+}Fe^{2+}$–(OH),F
	$Fe^{2+}Fe^{2+}Fe^{2+}$–(OH),F
$R^{2+}R^{2+}R^{3+}$–(OH),F	MgMgAl–(OH),F
	$MgMgFe^{3+}$–(OH),F
	$MgFe^{2+}$Al–(OH),F
	$MgFe^{2+}Fe^{3+}$–(OH),F
$R^{2+}R^{3+}R^{3+}$–O^{2-}	MgAlAl–O^{2-}
	$MgAlFe^{3+}$–O^{2-}
	$MgFe^{3+}Fe^{3+}$–O^{2-}
$R^{3+}R^{3+}R^{3+}$–O^{2-}	AlAlAl–O^{2-}
	$AlAlFe^{3+}$–O^{2-}
	$AlFe^{3+}Fe^{3+}$–O^{2-}
	$Fe^{3+}Fe^{3+}Fe^{3+}$–O^{2-}
$R^{1+}R^{1+}R^{3+}$–(OH),F	LiLiAl–(OH),F
	$LiLiFe^{3+}$–(OH),F
$R^{1+}R^{2+}R^{3+}$–(OH),F	LiMgAl–(OH),F
	$LiMgFe^{3+}$–(OH),F
	$LiFe^{2+}$Al–(OH),F
	$LiFe^{2+}Fe^{3+}$–(OH),F
$R^{1+}R^{3+}R^{3+}$–(OH),F	LiAlAl–(OH),F
	$LiAlFe^{3+}$–(OH),F
	$LiFe^{3+}Fe^{3+}$–(OH),F

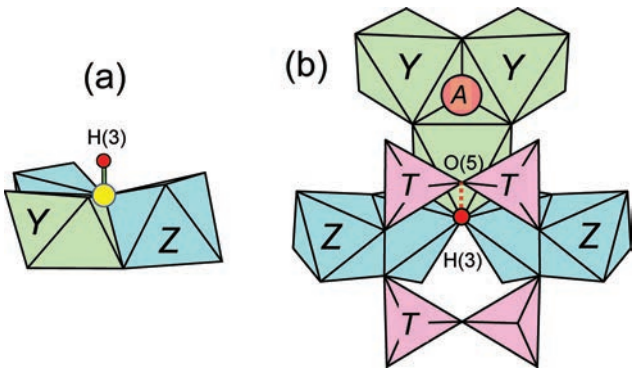

Fig. 17. The environment of the O(3) site in the tourmaline structure; (a) perspective view showing the nearest-neighbour cluster of *YZZ* octahedra; (b) view down **b** showing the H(1)...O(5) hydrogen bond; legend as in Fig. 15; red circle, H(3) atom; blue octahedra, *Z* octahedra.

nearest-neighbour octahedra (Fig. 17a) with the H(3) site situated ~0.97 Å from the O(3) site (Gatta *et al*., 2014). The H(3) ion hydrogen-bonds to O(5) (Fig. 17b), one of the bridging anions of the six-membered ring of tetrahedra, again suggesting that there will be next-nearest-neighbour effects arising from Si–O–Si, Si–O–Al and Si–O–B arrangements involving the acceptor anion. Moreover, the hydrogen bond involving H(3) is much stronger than those involving H(1). The H(3)–*X* distance is ~3.70 Å with little possibility of a significant interaction. A feature of particular importance with regard to the local coordination of the O

Table 4. Charge arrangements in accord with the valence-sum rule at O(3), plus possible chemical arrangements.

Charge arrangement [*YZZ*]–O(3)	Chemical arrangement [*YZZ*]–O(3)
$R^{1+}R^{3+}R^{3+}$–(OH)	MgAlAl–(OH)
	$MgAlFe^{3+}$–(OH)
	$MgFe^{3+}Fe^{3+}$–(OH)
	$Fe^{2+}Fe^{3+}Fe^{3+}$–(OH)
$R^{2+}R^{2+}R^{3+}$–(OH)	MgMgAl–(OH)
	$MgMgFe^{3+}$–(OH)
	$MgFe^{2+}Al$–(OH)
	$MgFe^{2+}Fe^{3+}$–(OH)
$R^{2+}R^{3+}R^{3+}$–O^{2-}	MgAlAl–O^{2-}
	$MgAlFe^{3+}$–O^{2-}
	$MgFe^{3+}Fe^{3+}$–O^{2-}
$R^{3+}R^{3+}R^{3+}$–O^{2-}	AlAlAl–O^{2-}
	$AlAlFe^{3+}$–O^{2-}
	$AlFe^{3+}Fe^{3+}$–O^{2-}
	$Fe^{3+}Fe^{3+}Fe^{3+}$–O^{2-}
$R^{1+}R^{2+}R^{3+}$–(OH)	LiMgAl–(OH)
	$LiMgFe^{3+}$–(OH)
	$LiFe^{2+}Al$–(OH)
	$LiFe^{2+}Fe^{3+}$–(OH)
$R^{1+}R^{3+}R^{3+}$–(OH)	LiAlAl–(OH)
	$LiAlFe^{3+}$–(OH)
	$LiFe^{3+}Fe^{3+}$–(OH)

(3) site is the disorder of divalent cations over the *Y* and *Z* sites. As noted above, both Mg (Hawthorne *et al*., 1993; Bosi & Lucchesi, 2004; Bosi *et al*., 2004) and Fe^{2+} (Bosi & Andreozzi, 2013) can be strongly disordered over *Y* and *Z*. As the O(3) site is coordinated by one *Y* and two *Z* sites, such disorder has a major effect on the incident bond-valence at O(3). Table 4 lists the possible local charge arrangements around the O(3) site as indicated by adherence to the valence-sum rule, together with the corresponding cation-anion arrangements.

6.3. Vibrational spectra and local arrangements in tourmaline

There has been a considerable amount of work on this issue. Although there is broad agreement that the intense lower-frequency absorptions are due to the (OH) group at O(3), there are significant differences in the details of these assignments, a situation that resembles the state of affairs in amphiboles prior to the work of Della Ventura and his colleagues beginning in the late 1990s. For amphiboles, the situation was clarified by an extensive program of synthesis and spectroscopy (sometimes coupled with Rietveld refinement, electron-microprobe analysis and HRTEM) that allowed identification of nearest-neighbour arrangements and next-nearest-neighbour effects in the spectra of chemically simple solid-solutions. From a structural perspective, the situation in tourmaline is even more complicated as there are two anion sites that commonly contain (OH). Moreover, the nearest-neighbour arrangement in tourmaline is topologically the same as the nearest-neighbour arrangement in amphibole, and hence one expects similar stereochemical effects.

In terms of next-nearest-neighbour effects, the O–H-stretching frequency in amphibole is strongly affected by (1) the occupancy of the *A* site by □, Na and Ca; (2) the coordination of the acceptor anion by different *T* cations: Si–O(7)–Si and Si–O(7)–Al; (3) the occupancy of the *M*(1,2,3) octahedra that share edges with nearest-neighbour octahedra; (4) replacement of (OH) by F in *A*-site-occupied amphiboles. In terms of the tourmaline structure:

6.3.1. Occupancy of the X-site

The *X*–H(1) distance is ~2.36 Å and *X*–O(1) distance is ~3.32 Å, and by analogy with the amphiboles, there should be a significant interaction between H(1) and the cation at the locally associated *X* site. Recent work has shown this to be the case. Berryman *et al*. (2016) assign Raman bands at 3817, 3777 and 3657–3667 cm^{-1} to the local arrangements $^{Y}Mg^{Y}Mg^{Y}Mg$–$^{O(1)}$(OH)–*X* where *X* = K, Na and □, respectively (Table 5). The corresponding frequency shifts from *X* = K to Na to □ are 40 and 115 cm^{-1}, significantly different from the analogous frequency differences in amphiboles which are as follows: *A* = K to Na to □ are ~5 and ~55 cm^{-1} (Hawthorne & Della Ventura, 2007), indicating that we must be careful in making quantitative analogies between amphiboles and tourmalines. For the local arrangements $^{Y}Mg^{Y}Mg^{Y}Al$–$^{O(1)}$(OH)–*X* and $^{Y}Mg^{Y}Al^{Y}Al$–$^{O(1)}$(OH)–*X* where *X* = Na and □, respectively (Table 5), the corresponding frequency shifts from *X* = Na to □ are 97 and ~98 cm^{-1}, significantly different from the corresponding shift of 115 $cm^{-1}$for $^{Y}Mg^{Y}Mg^{Y}Mg$–$^{O(1)}$(OH)–*X*, showing that even within a single tourmaline sample, one cannot absolutely associate specific frequency differences with particular substitutions. I note that the use of synthetic tourmaline samples, as was done by Berryman *et al*. (2016), greatly helps in the accurate assignment of bands.

6.3.2. Occupancy of the T-site

In amphibole, the coordination of the acceptor anion, O(7), may be Si–O–Si or Si–O–Al, and this produces a difference of ~20 cm^{-1} in the O–H-stretching frequency (Della Ventura *et al*., 1999). The corresponding acceptor anions in tourmaline may show the coordination Si–O–Si, Si–O–Al and Si–O–B, and similar next-nearest-neighbour effects might be expected in tourmaline. As noted above, the H(1) ion weakly hydrogen-bonds to the O(4) and O(5) anions (Gatta *et al*., 2014) (Fig. 15b and c), suggesting that substitution of Al for Si at the *T* site may shift the principal-stretching frequency for $^{O(1)}$(OH) to lower energies. Watenphul *et al*. (2016) report bands at 3720 and 3726 cm^{-1} in the Raman spectra of schorl and foitite, and assign these bands to the local arrangement $^{Y}Fe^{Y}Fe^{Y}Al$–$^{O(1)}$(OH)–^{X}Na, and a band at 3679 cm^{-1} in the spectrum of adachiite, ideally $CaFe_3Al_6(Si_5AlO_{18})(BO_3)_3(OH)_3(OH)$, that they also assign to the local arrangement $^{Y}Fe^{Y}Fe^{Y}Al$–$^{O(1)}$(OH)–^{X}Na ($+^{Y}Mg^{Y}Mg^{Y}Al$–$^{O(1)}$(OH)–^{X}Na). Here we see the effect of Al → Si substitution on the principal-stretching frequency for $^{O(1)}$(OH): a decrease of 44 cm^{-1}; again we

see a significant difference from the corresponding effect in amphibole where the difference in frequency is ~20 cm^{-1}.

6.3.3. *Occupancy of the Y- and Z-sites*

The nearest-neighbour octahedra for both O(1) and O(3) share edges with other *Y* and *Z* octahedra that may show local variations in cations from Li to R^{3+} (Al, Fe^{3+}, Cr^{3+}, V^{3+}), and fine structure is to be expected in the major bands in the infrared spectra. Most work on the vibrational spectra of tourmaline has assumed that each distinct local arrangement of atoms around a specific (OH) group will give rise to a distinct spectral signal (as is the case in amphibole), and peak assignment was done on this basis. This is the case for the (OH) group occupying the O(1) site. Table 5 summarizes the assignment of infrared and Raman bands to local arrangements involving (OH) at the O(1) site. There are many inconsistences with regard to band assignment; for example, the arrangement $^{Y}Mg^{Y}Mg^{Y}Mg$–$^{O(1)}$(OH)–^{X}Na is assigned to bands at ~3638 and ~3777 cm^{-1}, although the systematics of the data indicate that the latter value is correct. Similarly, the arrangement $^{Y}Li^{Y}Fe^{Y}Al$–$^{O(1)}$(OH)–^{X}Na is assigned to bands at ~3692 and 3585–3592 cm^{-1}. In principle, such differences could be due to next-nearest-neighbour effects, but the magnitude of the differences and the similarity in chemical composition do not suggest that this is the case. Many of the assignments do not incorporate the local occupancy of the *X* site, although these may be derived from the formulae of the tourmalines examined (these local occupancies are shown in italics in Table 5). The work of Berryman *et al*. (2016) shows the effectiveness of synthesis of simple compositions in band assignment, particularly when variation in next-nearest-neighbours has a significant effect on band position.

Most assignment of bands involving (OH) at the O(3) site has also assumed that each distinct local arrangement of atoms will give rise to a distinct spectral signal. However, Watenphul *et al*. (2016) used site-symmetry analysis (*e.g*., McMillan & Hess, 1988) to show that for the (OH) group occupying the O(3) site, the three H atoms related by rotation around the 3-fold axis collectively participate in a single phonon mode, and hence the energy of the principal O–H-stretching band is affected by the local cation arrangements associated with all three of the $^{O(3)}$(OH) groups, *i.e*. *YZZ–YZZ–YZZ*. They considered the assignment of cations over this configuration symbol without distinguishing between the *Y* and *Z* sites, *i.e*., assuming that the arrangements involving $^{Y}Mg^{Z}Al^{Z}Al$ and $^{Y}Al^{Z}Mg^{Z}Al$, for example, give rise to bands that are energetically indistinguishable. This assumption leads to a consistent assignment of Raman bands in a wide compositional range of tourmalines (Watenphul *et al*., 2016). Bosi *et al*. (2016a) and b) use this model to assign infrared bands in several tourmalines that are in accord with the assignments from Raman spectroscopy. Moreover, they identify next-nearest-neighbour effects with regard to bands assigned to $^{O(3)}$(OH), assigning bands to extended arrangements that include the character of the anion at the neighbouring O(1) site: (OH),F versus O^{2-}. I do not list infrared and Raman bands assigned to local arrangements involving $^{O(3)}$(OH) as (1) according to the arguments of Watenphul *et al*. (2016), many of these assignments

Table 5. Local arrangements around the O(1) = (OH) site and assigned bands in the infrared and Raman spectra.

X	*Y*	*Y*	*Y*	Infrared wavelength (cm^{-1})	Ref.	Raman wavelength (cm^{-1})	Ref.
K	Mg	Mg	Mg		—	3817	a
Na	Mg	Mg	Mg	3738, 3739, 3777	(1), (2), (3), (4), (5)	3776–3778, 3770	a, b
K	Mg	Mg	Al		—	3769	a
Na	Mg	Mg	Al	3634, 3738–3740	(2), (4), (5)	3739–3740, 3739 + 3679	a, b
Na	Mg	Al	Al			3723	a
□	Mg	Mg	Mg	3677, 3677	(2), (5)	3657–3667	a
□	Mg	Mg	Al	3644, 3642–3643	(4), (5)	3636–3650, 3668	a, b
□	Mg	Al	Al			3618–3632, 3639	a, b
Ca	Mg	Mg	Mg			3627–3635	c
Na	R^{2+}	R^{2+}	R^{3+}	3720	(7)		
Na	Li	Fe	Al	3692	(1)		
Ca	Li	Al	Al	3680	(1)		
Na	Li	Al	Al	3650, 3657	(1), (6)	3657	d
Na	Li	Mn	Al	3670	(1)		
Na	□	R^{3+}	R^{3+}	3560	(7)		
Na	Li,Al	Al	Al	3641–3646	(8)		
Na	Fe	Fe	Fe	3633	(1)		
Na	Fe	Fe	R^{2+}	3628–3635	(8)		
Na	Li	Fe	Al	3585–3592	(8)		
Na	Mg,R^{3+}	Mg	Mg	3710–3720	(4), (5)		
Na	Li	Al	R	3594	(8)		

References, infrared: (1) Gonzalez-Carreño *et al*. (1988); (2) Gourdant & Robert (1997); (3) Bosi *et al.* (2015); (4) Bosi *et al*. (2016a); (5) Bosi *et al*. (2016b); (6) Skogby *et al*. (2012); (7) Filip *et al*. (2012); (8) Castañeda *et al*. (2000).
References, Raman: (a) Berryman *et al*. (2016); (b) Watenphul *et al*. (2016); (c) Fantini *et al*. (2014); (d) Skogby *et al*. (2012).

cannot be correct, and (2) reassignment must involve detailed inspection of the spectra and chemical formulae of the tourmalines involved.

At some stage, it is probable that we will need more extensive configuration symbols for the O(1) and O(3) sites, but to write these seems premature at the moment. Moreover, if the collective phonon mode of triplets of neighbouring $^{O(3)}$(OH) groups also energetically averages *Y* and *Z* sites, we cannot distinguish between arrangements involving, for example, $^{Y}Mg^{Z}Al^{Z}Al$ and $^{Y}Al^{Z}Mg^{Z}Al$ by Raman spectroscopy. A program of systematic synthesis of tourmaline solid-solutions, together with their characterization by infrared and Raman spectroscopy, would help resolve some of the current ambiguities in the assignment of bands and the identification of local structural arrangements.

7. Short-range order-disorder in pyroxenes

The chemical formula of the pyroxene-supergroup minerals may be written very generally (Morimoto *et al*., 1989) as:

$$M2M1T_2O_6$$

where

M2 = Li, Na, Mg, Fe^{2+}, Mn^{2+} and Ca;
M1 = Mg, Fe^{2+}, Mn^{2+}, Al, Fe^{3+}, V^{3+}, Cr^{3+};
T = Si, Al, Fe^{3+}.

Here, I will focus on the monoclinic pyroxenes with *C*2/*c* symmetry in which the M2, M1 and T groups of cations occupy the *M*(2), *M*(1) and *T* sites.

In the pyroxene structure, there are three distinct cation sites and three distinct anion sites, and each anion coordinates all three cation sites. Hence any heterovalent changes in composition affect all anion sites in the structure. ^{29}Si MAS NMR spectroscopy is effective in examining short-range arrangements involving Si and Al in the pyroxene structure, and Fig. 18a depicts the arrangement of nearest-neighbour-cation sites/polyhedra around a specific *T* tetrahedron. The central *T* tetrahedron shares corners with adjacent *T* tetrahedra within the same chain. It also shares edges with two *M*(2) polyhedra, corners with two *M*(2) polyhedra, and corners with three *M*(1) octahedra. We may write a site-configuration symbol for the *T* site in pyroxene in exactly the same way that we did for amphibole:

$$\text{Si–}TT\text{–}M(2)M(2)\text{–}M(1)M(1)\text{–M(1)–}M(2)M(2)$$

where the pair of *T* sites are nearest-neighbour-cation sites along the tetrahedron chain, the first pair of *M*(2) sites each share two bonds (a polyhedron edge) with anions of the central *T*(=Si) tetrahedron, the pair of *M*(1) sites each share a [4]-coordinated anion with the central *T*(=Si) tetrahedron, the single *M*(1) site shares a [3]-coordinated anion with the central *T*(=Si) tetrahedron, and the second pair of *M*(2) sites each share a single anion (a polyhedron corner) with the central *T*(=Si) tetrahedron. Thus end-member diopside would have the local arrangement Si–SiSi–CaCa–MgMg–Mg–CaCa, end-member jadeite would have the local arrangement Si–SiSi–NaNa–AlAl–Al–NaNa, and completely short-range-ordered kushiroite (Kimura *et al*., 2009) would have the local arrangement Si–AlAl–CaCa–AlAl–Al–CaCa. The linkage of the [3]- and [4]-coordinated anions to the *M*(1) cation has been separated here because the strengths of the chemical bonds involved are quite different and it is possible (although as yet unknown) that different occupancy of the sites involved could give rise to separate spectral signals.

Figure 18b shows the arrangement of nearest-neighbour-cation sites/polyhedra around a specific *M*(1) octahedron. The central *M*(1) octahedron shares edges with two adjacent *M*(1) octahedra along the same octahedron chain. It also shares corners with six *T* tetrahedra, edges with two *M*(2) polyhedra and corners with two *M*(2) polyhedra. We may write a site-configuration symbol for the *M*(1) site in

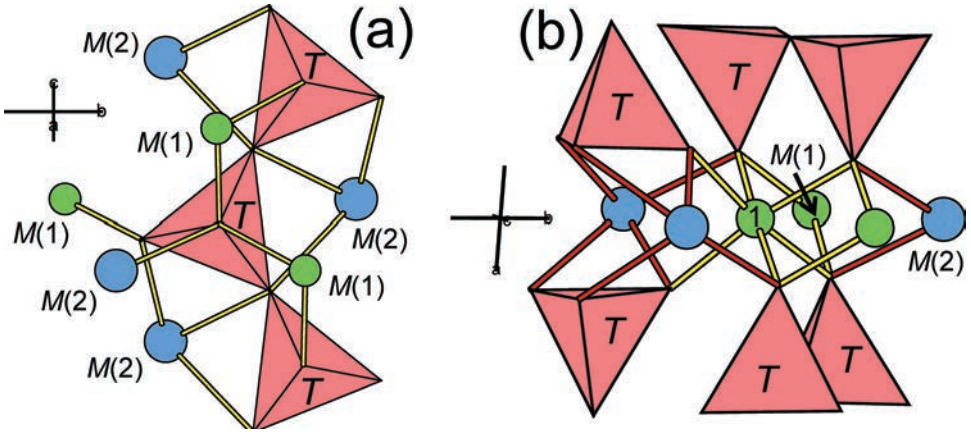

Fig. 18. (a) A fragment of the chain of tetrahedra in the *C*2/*c* pyroxene structure, together with the next-nearest-neighbour cation sites of the central tetrahedron; (b) a fragment of the *C*2/*c* pyroxene structure centered on the *M*(1) site, together with the next-nearest-neighbour cation sites of the central octahedron; pink, *T* tetrahedra; small green circles, *M*(1) sites; large blue circles, *M*(2) sites.

pyroxene:

$$M(1)\text{–}M(1)M(1)\text{–}TT.T.TT.T\text{–}M(2)M(2)M(2).$$

Adjacent *T* sites link to each other; *T* sites separated by dots do not link together; thus in Fig. 18b, *TT.T* occurs both above and below the central *M*(1) (=Al) site. Hence end-member diopside will have the local arrangement Mg–MgMg–SiSi.Si.SiSi.Si–CaCaCa, end-member jadeite will have the local arrangement Al–AlAl–SiSi.Si.SiSi. Si–NaNaNa, and completely short-range-ordered kushiroite will have the local arrangement Al–AlAl–SiAl.*T*. AlSi.*T*–CaCaCa where *T* = Si or Al. The reason for distinguishing between monomers and dimers of tetrahedra in this local arrangement is as follows: the probability that the monomer sites are occupied by Si or Al is the Si:Al ratio of the mineral; the probabilities that the dimers are occupied by SiSi, SiAl and AlAl are very heavily weighted in favour of SiAl (as indicated by the ^{29}Si MAS NMR spectrum of kushiroite, Flemming & Luth, 2002). Thus the configuration symbol given above can accommodate solid solution at all three cation sites in the *C*2/*c* pyroxene structure.

7.1. MAS NMR spectra and local arrangements in pyroxene

There has not been a lot of work on short-range arrangements in pyroxene. Flemming & Luth (2002) examined Si-^{T}Al arrangements in synthetic pyroxenes along the join diopside–kushiroite: $CaMgSi_2O_6$–$CaAl(AlSi)O_6$, by ^{29}Si MAS NMR spectroscopy. There are three possible nearest-neighbour arrangements for Si along the pyroxene chain: Si–Si–Si, Al–Si–Si, Al–Si–Al. In synthetic diopside, only Si–Si–Si is possible. In solid solutions, the pyroxene chain must be a mixture of arrangements. In synthetic kushiroite, the pyroxene chain may consist only of Al–Si–Al arrangements, but it may also consist of a mixture of arrangements. Figure 19 shows the ^{29}Si MAS NMR spectra for synthetic pyroxenes along the diopside–kushiroite join taken from Flemming & Luth (2002). The Di_{100} composition shows a single peak at −84.4 ppm consistent with the single local arrangement Si–Si–Si. The Ku_{100} composition shows three peaks at −84.4, −85.6 and −89.7 ppm, consistent with the three possible local arrangements Si–Si–Si, Al–Si–Si and Al–Si–Al. Moreover, we know that the *M*(1) site is completely occupied by Al, and hence additional local arrangements involving *M*(1) are not possible. Thus we know that Ku_{100} does not show a completely short-range-ordered arrangement (Al–Si–Al) along the tetrahedron chain. Flemming & Luth (2002) were concerned that $CaAl(AlSi)O_6$ with the three local arrangements Si–Si–Si, Al–Si–Si and Al–Si–Al in the pyroxene chain must also contain Al–Al linkages, a situation which violates Löwenstein's rule (Löwenstein, 1954). This is not an issue. Whether or not Al–O–Al linkages may occur depends on the valence-sum rule in the structural arrangement of interest: Al–O–Al linkages will not occur where the interstitial cations have too low a Lewis acidity to satisfy the valence-sum rule at the linking cation, and Al–O–Al linkages may occur where the interstitial cations have sufficient Lewis acidity to satisfy the valence-sum rule at the linking cation; thus, for example, krotite, $CaAl_2O_4$ (Ma *et al*., 2011) has $^{[4]}$Al–O–$^{[4]}$Al linkages because the central anion is also bonded to two Ca atoms that provide sufficient bond-valence to satisfy the valence-sum rule. Thus one expects $^{[4]}$Al–O–$^{[4]}$Al linkages to occur in kushiroite because the presence of two Ca atoms linked to the bridging anion, together with the flexibility of the pyroxene structure, allows accord with the valence-sum rule at the bridging anion.

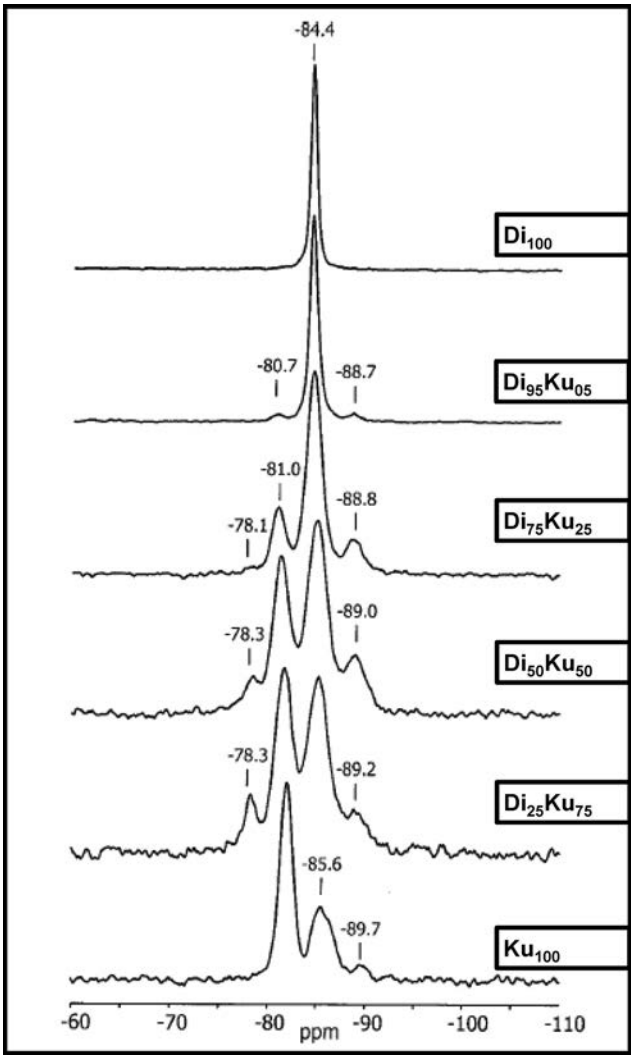

Fig. 19. ^{29}Si MAS NMR spectra for compositions along the join synthetic diopside–kushiroite; numbers indicate the chemical shift in ppm. Modified after Flemming & Luth (2002).

Flemming *et al*. (2015) re-examined this issue using ^{27}Al MAS NMR and ^{27}Al triple-quantum (3Q) MAS NMR spectroscopy at ultra-high field, combined with computational simulations. Figure 20a shows the ^{27}Al MAS NMR spectra of synthetic kushiroite measured at 14.1 and 21.1 T. Both spectra show two envelopes, one with two maxima and one with one maximum and a shoulder, but there is considerable reduction in peakwidth

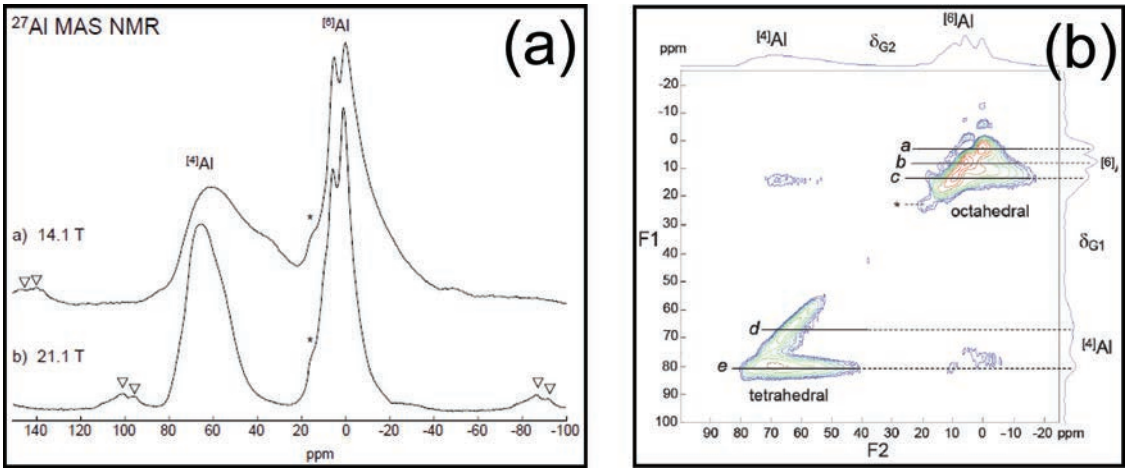

Fig. 20. ^{27}Al MAS NMR spectra of kushiroite; (a) upper: at 14.1 T; lower: at 21.1 T. The inverted triangles indicate spinning sidebands, the * indicates a signal from Al_2O_3; (b) two-dimensional 3Q MAS NMR spectrum at 21.1 T. The ordinate shows the 3Q projection, the abscissa shows the MAS NMR projection. Sections through the spectrum are labelled *a-e*, see Fig. 21; modified from Flemming *et al*. (2015).

at higher field. The doublet at ~0–5 ppm is due to $^{[6]}$Al and the peak at ~60–65 ppm is due to $^{[4]}$Al. In terms of the configuration symbol derived for *M*(1) above: *M*(1)–*M*(1)*M*(1)–*TTTTTT*–*M*(2)*M*(2)M(2), *M*(1) = Al and *M*(2) = Ca, and the symbol may be reduced to Al–AlAl–*TT.T.TT.T*–CaCaCa. Figure 20b shows the 3Q MAS NMR spectrum of kushiroite at 21.1 T. There is significant resolution along the F1 axis, and the sections through the peaks in Fig. 20b are shown in Fig. 21. The $^{[6]}$Al sections (Fig. 21a–c) were interpreted as three distinct arrangements of ^{T}Al and ^{T}Si around $^{M(1)}$Al: a, 2Al + 4Si; b, 3Al + 3Si; c, 4Al + 2Si by Flemming *et al*. (2015). If we look at the M(1) configuration symbol above, *M*(1) = Al and *M*(2) = Ca and the symbol becomes Al–AlAl–*TT.T.TT.T*–CaCaCa. From the ^{29}Si MAS NMR spectrum of synthetic kushiroite (Fig. 19, bottom) of Flemming & Luth (2002), pairs of locally adjacent tetrahedra are dominated by the arrangement AlSi, and hence the dominant local arrangements are as follows:

(1) Al–AlAl–AlSi.Al.AlSi.Al–CaCaCa = 4^{T}Al + 2^{T}Si
(2) Al–AlAl–AlSi.Al.AlSi.Si–CaCaCa = 3^{T}Al + 3^{T}Si

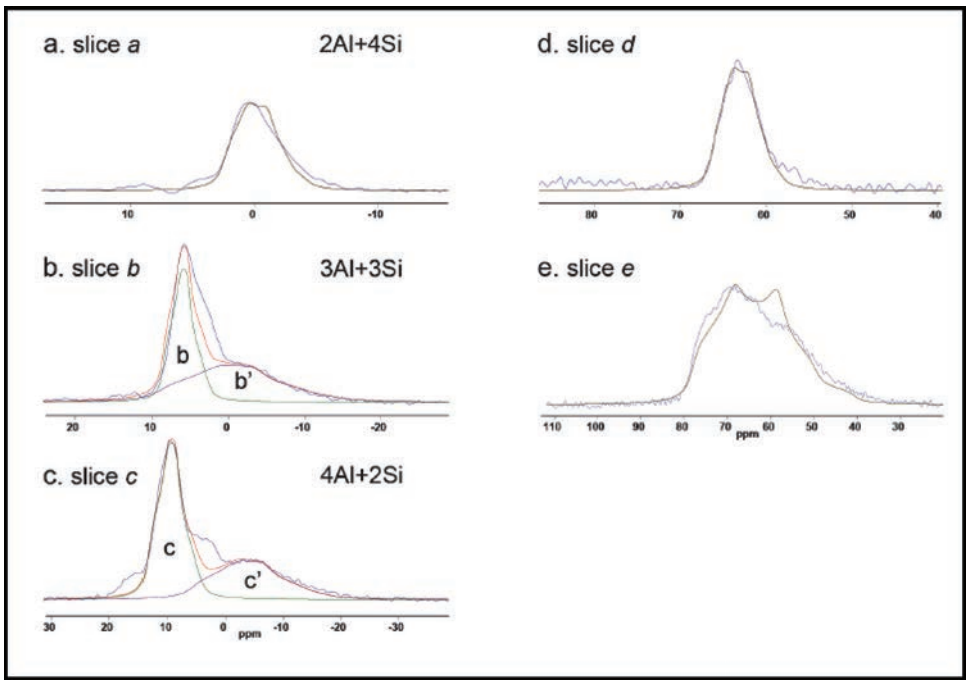

Fig. 21. One-dimensional slices through slices *a-e* in Fig. 20; modified from Flemming *et al*. (2015).

(3) Al–AlAl–AlSi.Si.AlSi.Si–CaCaCa = 2^{T}Al + 4^{T}Si.

However, Flemming & Luth (2002) show that the frequency of occurrence of the arrangements Al–Si–Al, Al–Si–Si and Si–Si–Si is 0.70:0.25:0.05. From this result, we may calculate the frequency of the pairs AlSi, SiSi and AlAl as 0.70:0.15:0.15. Thus the probability of one TT pair in the configuration symbol being SiSi or AlAl is 0.15, and hence arrangements containing one such pair are relatively common:

(4) Al–AlAl–SiSi.Al.AlSi.Al–CaCaCa = 3^{T}Al + 3^{T}Si
(5) Al–AlAl–SiSi.Al.AlSi.Si–CaCaCa = 2^{T}Al + 4^{T}Si
(6) Al–AlAl–SiSi.Si.AlSi.Si–CaCaCa = 1^{T}Al + 5^{T}Si
(7) Al–AlAl–AlAl.Al.AlSi.Al–CaCaCa = 5^{T}Al + 1^{T}Si
(8) Al–AlAl–AlAl.Al.AlSi.Si–CaCaCa = 4^{T}Al + 2^{T}Si
(9) Al–AlAl–AlAl.Si.AlSi.Si–CaCaCa = 3^{T}Al + 3^{T}Si.

Thus we have numerous possible local arrangements that will occur with a reasonably high frequency. Using the pair-frequency values AlSi:SiSi:AlAl = 0.70:0.15:0.15, we may calculate the frequency of the various compositions of the arrangements as follows:

5^{T}Al + 1^{T}Si = 0.050
4^{T}Al + 2^{T}Si = 0.283
3^{T}Al + 3^{T}Si = 0.333
2^{T}Al + 4^{T}Si = 0.283
1^{T}Al + 5^{T}Si = 0.050.

8. How to deal with structural and spectral complexity

It is apparent from the above discussion that it is not a simple task to assign specific spectral signals to particular local atomic arrangements. There has been a lot of work on this issue with regard to amphiboles, and this work provides a model for how to deal with this issue in other (super) groups of minerals. Synthesis of simple amphibole compositions (*e.g.*, Robert & Della Ventura, 1989; Della Ventura & Robert, 1990; Mottana *et al.*, 1990) allowed unambiguous identification and assignment of spectral features, and gradual synthesis of more complex synthetic solid-solutions involving end-member compositions with well-characterized spectral and crystallographic properties allowed band assignment for more complicated solid-solutions. This issue was discussed by Della Ventura *et al.* (1999) who synthesized amphiboles along the richterite–pargasite join. The spectrum of synthetic richterite is well understood, and so this gives us a start in spectrum fitting and assignment. The general approach here is to fit one model to all the spectra of the series, as in this way we can considerably increase the number of observations without greatly increasing the number of fitting parameters. We can identify the key features of this approach as follows: (1) numerical fitting of the spectra to component bands must be congruent for all spectra; (2) the intensities of the component bands must vary systematically with changes in chemical composition; (3) the variations in ordering derived from the spectral assignments must be in accord with the variation in cell dimensions across the series. It seems apparent that this is the way to proceed if the very complicated compositions of general interest are to be understood with a reasonable degree of confidence.

Several spectral studies have assigned bands by assuming that short-range arrangements are random and that their frequencies of occurrence may be calculated on the basis of a random distribution of ion species over the relevant sites. This assumption is not generally correct as it ignores the constraint of the valence-sum rule (Brown, 2002) on local arrangements. Thus the arrangements ^{Y}Al^{Y}Al^{Y}Al–$^{O(1)}$(OH) and ^{Y}Mg^{Z}Mg^{Z}Mg–$^{O(3)}$(OH) cannot occur in tourmaline (Hawthorne, 1996, 2002; Bosi, 2011, 2013) as they violate the local version of the valence-sum rule (Hawthorne, 1997). Local order may occur in structures, and frequencies of occurrence of local arrangements cannot be reliably calculated assuming a statistical distributions of ions.

9. Summary

The derivation of local arrangements in minerals is a very difficult experimental problem. It requires a combination of crystallography, spectroscopy and theory: Crystallography gives us the average atomic arrangement in a mineral, and crystal-chemical information that may be deconvoluted into probable local stereochemical details; spectroscopy gives us local signals that may be correlated with crystal-structure information to identify local atomic arrangements, and theory allows calculations pertaining to results that may indicate whether or not they are reasonable from the perspectives of crystal chemistry and chemical bonding. Here, I have discussed some aspects of local arrangements in amphiboles, tourmalines and pyroxenes. It is apparent that these issues are very complicated, particularly with regard to spectral resolution and interpretation. A helpful approach to this problem is the *a priori* use of *configuration symbols* that identify the surrounding sites and/or coordination polyhedra that may affect spectral features via occupancy of different species, *i.e.*, the *local atomic arrangements*, as the configuration symbols include all crystal-chemical details that may affect the behaviour of the spectroscopic probe. The high degree of complexity of many of these minerals and their corresponding spectra warrant systematic synthesis of simple compositions and solid solutions, coupled with their characterization by a combination of spectroscopic, crystallographic and analytical methods; this approach should give us a much better knowledge of the short-range arrangements of atoms in complex solid-solutions.

Acknowledgements: I thank Elena Sokolova for encouraging me to write this paper and for providing some very important advice, and I thank Ferdinando Bosi and Gianni Andreozzi for the invitation to come to Rome and speak on this topic. This work was supported by a Natural Sciences and Engineering Research Council of Canada Discovery grant to FCH.

References

Addison, W.E. & Sharp, J.H. (1962): Amphiboles III. The reduction of crocidolite. *J. Chem. Soc.*, **1962**, 3693–3698.

Addison, C.C., Addison, W.E., Neal, G.H., Sharp, J.H. (1962a): Amphiboles. I. The oxidation of crocidolite. *J. Chem. Soc.*, **1962**, 1468–1471.

Addison, W.E., Neal, G.H., Sharp, J.H. (1962b): Amphiboles. II. The kinetics of the oxidation of crocidolite. *J. Chem. Soc.*, **1962**, 1472–1475.

Berryman, E.J., Wunder, B., Ertl, A., Koch-Müller, M., Rhede, D., Scheidl, K., Giester, G., Heinrich, W. (2016): Influence of the *X*-site composition on tourmaline's crystal structure: investigation of synthetic K-dravite, dravite, oxy-uvite, and magnesio-foitite using SREF and Raman spectroscopy. *Phys. Chem. Minerals*, **43**, 83–102.

Boschmann, K., Burns, P.C., Hawthorne, F.C., Raudsepp, M., Turnock, A.C. (1994): A-site disorder in synthetic fluor-edenite, a crystal structure study. *Can. Mineral.*, **32**, 21–30.

Bosenick, A., Dove, M.T., Geiger, C.A. (2000): Simulation studies on the pyrope-grossular garnet solid solution. *Phys. Chem. Minerals*, **27**, 398–418.

Bosi, F. (2011): Stereochemical constraints in tourmaline: from a short-range to a long-range structure. *Can. Mineral.*, **49**, 17–27.

— (2013): Bond-valence constraints around the O1 site of tourmaline. *Mineral. Mag.*, **77**, 343–351.

Bosi, F. & Andreozzi, G.B. (2013): A critical comment on Ertl et al. (2012): "Limitations of Fe^{2+} and Mn^{2+} site occupancy in tourmaline: Evidence from Fe^{2+}- and Mn^{2+}-rich tourmaline. *Am. Mineral.*, **98**, 2183–2192.

Bosi, F. & Lucchesi, S. (2004): Crystal chemistry of the schorl-dravite series. *Eur. J. Mineral.*, **16**, 335–344.

—, — (2007): Crystal chemical relationships in the tourmaline group: structural constraints on chemical variability. *Am. Mineral.*, **92**, 1054–1063.

Bosi, F., Lucchesi, S., Reznitskii, L. (2004): Crystal chemistry of the dravite-chromdravite series. *Eur. J. Mineral.*, **16**, 345–352.

Bosi, F., Skogby, H., Balić-Žunić, T. (2016a): Thermal stability of extended clusters in dravite: a combined EMP, SREF and FTIR Study. *Phys. Chem. Minerals*, DOI 10.1007/s00269–016-0804-y.

Bosi, F., Skogby, H, Hålenius, U. (2016b): Thermally induced cation redistribution in Fe-bearing oxy-dravite and potential geothermometric implications. *Contr. Mineral. Petrol.*, (in review).

Brown, I.D. (2002): The chemical bond in inorganic chemistry. The bond valence model. Oxford University Press.

— (2009): Recent developments in the methods and applications of the bond valence model. *Chem. Rev.*, **109**, 6858–6919.

Brown, I.D. & Shannon, R.D. (1973): Empirical bond-strength-bond-length curves for oxides. *Acta Crystallogr.*, **A29**, 266–282.

Burns, R.G. & Greaves, C.J. (1971): Correlations of infrared and Mossbauer site population measurements of actinolites. *Am. Mineral.*, **56**, 2010–2033.

Burns, P.C. & Hawthorne, F.C. (1994): Structure and hydrogen bonding in preobrazhenskite, a complex heteropolyhedral borate. *Can. Mineral.*, **32**, 387–396.

Burns, R.G. & Strens, R.G.J. (1966): Infrared study of the hydroxyl bands in clinoamphiboles. *Science*, **153**, 890–892.

Burns, P.C., MacDonald, D.J., Hawthorne, F.C. (1994): The crystal chemistry of manganese-bearing elbaite. *Can. Mineral.*, **32**, 31–41.

Cameron, M. & Papike, J.J. (1980): Crystal chemistry of silicate pyroxenes. *in* "Pyroxenes", C.T. Prewitt, ed. *Rev. Mineral.*, **7**, 5–92.

Castañeda, C., Oliveira, E.F., Gomes, N., Soares, A.C.P. (2000): Infrared study of OH in tourmaline from the elbaite-schorl series. *Am. Mineral.*, **85**, 1503–1507.

Chang, I.F. & Mitra, S.S. (1968): Application of a modified random-element-isodisplacement model to long-wavelength optic phonons of mixed crystals. *Phys. Rev.*, **172**, 924–933.

Clark, M.W. & Freeman, A.G. (1967): Kinetics and mechanism of dehydroxylation of crocidolite. *Trans. Farad. Soc.*, **63**, 2051–2056.

Della Ventura, G. & Robert, J.L. (1990): Synthesis, XRD and FTIR studies of strontium richterites. *Eur. J. Mineral.*, **2**, 171–176.

Della Ventura, G., Robert, J.-L., Hawthorne, F.C. (1996): Infrared spectroscopy of synthetic (Ni,Mg,Co)-potassium-richterite. *in* "Mineral spectroscopy: a tribute to Roger G. Burns", M.D. Dyar, C. McCammon, M.W. Schaefer, eds. The Geochemical Society Spec. Pub. No. 5, 55–63.

—, —, — (1998): Characterization of OH-F short-range order in potassium-fluor-richterite by infrared spectroscopy in the OH-stretching region. *Can. Mineral.*, **36**, 181–185.

Della Ventura, G., Hawthorne, F.C., Robert, J.-L., Delbove, F., Welch, M.F., Raudsepp, M. (1999): Short-range order of cations in synthetic amphiboles along the richterite-pargasite join. *Eur. J. Mineral.*, **11**, 79–94.

Della Ventura, G., Robert, J.-L., Sergent, J., Hawthorne, F.C., Delbove, F. (2001): Constraints on F vs. OH incorporation in synthetic $^{[6]}$Al-bearing in monoclinic amphiboles. *Eur. J. Mineral.*, **13**, 841–847.

Della Ventura, G., Marcelli, A., Bellatreccia, F. (2014a): SR-FTIR microscopy and FTIR imaging in the Earth sciences. *in* "Spectroscopic Methods in Mineralogy and Material Sciences", G.S. Henderson, D.R. Neuville, R.T. Downs, eds. *Rev. Mineral. Geochem.*, **78**, 447–480.

Della Ventura, G., Bellatreccia, F., Cámara, F., Oberti, R. (2014b): Crystal-chemistry and short-range order of fluoro-edenite and fluoro-pargasite: a combined X-ray diffraction and FTIR spectroscopic approach. *Mineral. Mag.*, **78**, 293–310.

Fantini, C., Tavares, M.C., Krambrock, K., Moreira, R.L., Righi, A. (2014): Raman and infrared study of hydroxyl sites in natural uvite, fluor-uvite, magnesio-foitite, dravite and albaite tourmalines. *Phys. Chem. Minerals*, **41**, 247–254.

Filip, J., Bosi, F., Novák, M., Skogby, H., Tuček, J., Cuda, J., Wildner, M. (2012): Iron redox reactions in the tourmaline structure: High-temperature treatment of Fe^{3+}-rich schorl. *Geochim. Cosmochim. Acta*, **86**, 239–256.

Flemming, R.L. & Luth, R.W. (2002): ^{29}Si MAS NMR study of diopside-Ca-Tschermak clinopyroxenes: Detecting both tetrahedral and octahedral Al. *Am. Mineral.*, **87**, 25–36.

Flemming, R.L., Terskikh, V., Ye, E. (2015): Aluminum environments in synthetic Ca-Tschermak clinopyroxene ($CaAlAlSiO_6$) from Rietveld refinement, ^{27}Al NMR, and first-principles calculations. *Am. Mineral.*, **100**, 2219–2230.

Freeman, C.L., Allan, N.L., van Westrenen, W. (2006): Local cation environments in the pyrope-grossular $Mg_3Al_2Si_3O_{12}$-$Ca_3Al_2Si_3O_{12}$ garnet solid solution. *Phys. Rev. B*, **74**, 1342031–1342039.

Gagné, O. & Hawthorne, F.C. (2015): Comprehensive derivation of bond-valence parameters for ion pairs involving oxygen. *Acta Crystallogr.*, **B71**, 562–578.

Gatta, G.D., Danisi, R.M., Adamo, I., Meven, M., Diella, V. (2012): A single-crystal neutron and X-ray diffraction study of elbaite. *Phys. Chem. Minerals*, **39**, 577–588.

Gatta, G.D., Bosi, F., Mcintyre, G.J., Skogby, H. (2014): First accurate location of two proton sites in tourmaline: A single-crystal neutron diffraction study of oxy-dravite. *Mineral. Mag.*, **78**, 681–692.

Gonzalez-Carreño, T., Fernfindez, M., Sanz, J. (1988): Infrared and electron microprobe analysis of tourmalines. *Phys. Chem. Minerals*, **15**, 452–460.

Gottschalk, M., Andrut, M., Melzer, S. (1999): The determination of cummingtonite content of synthetic tremolite. *Eur. J. Mineral.*, **11**, 967–982.

Gourdant, J.-P. & Robert, J.-L. (1997): Tourmalines in the system Na_2O-MgO-Al_2O_3-Ga_2O_3-B_2O_3-SiO_2-H_2O: an experimental and crystal-chemical investigation. *in* Tourmaline 1997: Int. Symp. on Tourmaline (Nové Městona Moravě, Czech Republics), 30–31 (abstr.).

Grice, J.D. & Ercit, T.S. (1993): Ordering of Fe and Mg in the tourmaline crystal structure: The correct formula. *N. Jb. Mineral. Abh.*, **165**, 245–266.

Groat, L.A., Hawthorne, F.C., Rossman, G.R., Ercit, T.S. (1995): The infrared spectroscopy of vesuvianite in the OH region. *Can. Mineral.*, **33**, 609–626.

Hawthorne, F.C. (1983a): Quantitative characterization of site-occupancies in minerals. *Am. Mineral.*, **68**, 287–306.

— (1983b): Characterization of the average structure of natural and synthetic amphiboles. *Period. Mineral.*, **52**, 543–581.

— (1983c): The crystal chemistry of the amphiboles. *Can. Mineral.*, **21**, 173–480.

— (1988): Spectroscopic methods in mineralogy and geochemistry (Ed.). *Rev. Mineral.*, **18**, 1–698.

— (1996): Structural mechanisms for light-element variations in tourmaline. *Can. Mineral.*, **34**, 123–132.

— (1997): Short-range order in amphiboles: a bond-valence approach. *Can. Mineral.*, **35**, 201–216.

— (2002): Bond-valence constraints on the chemical composition of tourmaline. *Can. Mineral.*, **40**, 789–797.

Hawthorne, F.C., Della Ventura, G. (2007): Short-range order in amphiboles. *in* "Amphiboles: Crystal Chemistry, Occurrence and Health Issues", F.C. Hawthorne, R. Oberti, G. Della Ventura, A. Mottana, eds. *Rev. Mineral. Geochem.*, **67**, 173–222.

Hawthorne, F.C. & Grundy, H.D. (1976): The crystal chemistry of the amphiboles. IV. X-ray and neutron refinements of the crystal structure of tremolite. *Can. Mineral.*, **14**, 334–345.

Hawthorne, F.C. & Oberti, R. (2007): Amphiboles: crystal chemistry. *in* "Amphiboles: Crystal Chemistry, Occurrence and Health Issues", F.C. Hawthorne, R. Oberti, G. Della Ventura, A. Mottana, eds. *Rev. Mineral. Geochem.*, **67**, 1–54.

Hawthorne, F.C. & Waychunas, G.A. (1988): Spectrum fitting methods. *in* "Spectroscopic Methods in Mineralogy and Geochemistry", F.C. Hawthorne, ed. *Rev. Mineral.*, **18**, 63–98.

Hawthorne, F.C., MacDonald, D.J., Burns, P.C. (1993): Reassignment of cation site-occupancies in tourmaline: Al/Mg disorder in the crystal structure of dravite. *Am. Mineral.*, **78**, 265–270.

Hawthorne, F.C., Della Ventura, G., Robert, J.-L. (1996a): Short-range order of (Na,K) and Al in tremolite: An infrared study. *Am. Mineral.*, **81**, 782–784.

Hawthorne, F.C., Oberti, R., Sardone, N. (1996b): Sodium at the A site in clinoamphiboles: the effects of composition on patterns of order. *Can. Mineral.*, **34**, 577–593.

Hawthorne, F.C., Welch, M.D., Della Ventura, G., Liu, S., Robert, J.-L., Jenkins, D.M. (2000): Short-range order in synthetic aluminous tremolites: An infrared and triple-quantum MAS NMR study. *Am. Mineral.*, **85**, 1716–1724.

Hawthorne, F.C., Della Ventura, G., Oberti, R., Robert, J.-L., Iezzi, G. (2005): Short-range order in minerals: amphiboles. *Can. Mineral.*, **43**, 1895–1920.

Hawthorne, F.C., Oberti, R., Harlow, G.E., Maresch, W., Martin, R.F., Schumacher, J.C., Welch, M.D. (2012): Nomenclature of the amphibole super-group. *Am. Mineral.*, **97**, 2031–2048.

Heavysege, D., Abdu, Y., Hawthorne, F.C. (2015): Long-range and short-range order in gem pargasite from Myanmar: Crystal structure refinements and infrared spectroscopy. *Can. Mineral*, **53**, 497–510.

Henderson, G.S., Neuville, D.N., Downs, R.T. (2014): Spectroscopic Methods in Mineralogy and Materials Science (Eds.) *Rev. Mineral. Geochem.*, **78**, 1–800.

Henry, D.J., Novák, M., Hawthorne, F.C., Ertl, A., Dutrow, B.L., Uher, P., Pezzotta, F. (2011): Nomenclature of the tourmaline super-group minerals. *Am. Mineral.*, **96**, 895–913.

Keen, D.A. & Goodwin, A.L. (2015): The crystallography of correlated disorder. *Nature*, **521**, 303–309.

Kimura, M., Mikouchi, T., Suzuki, A., Miyahara, M., Ohtani, E., Goresy, A.E. (2009): Kushiroite, $CaAlAlSiO_6$: A new mineral of the pyroxene group from the ALH 85085 CH chondrite, and its genetic significance in refractory inclusions. *Am. Mineral.*, **94**, 1479–1482.

Kirkpatrick, R.J. (1988): MAS NMR spectroscopy of minerals and glasses. *in* "Spectroscopic Methods in Mineralogy and Geochemistry", F.C. Hawthorne, ed. *Rev. Mineral.*, **18**, 341–403.

Leissner, L., Schlüter, J., Horn, I., Mihailova, B. (2015): Exploring the potential of Raman spectroscopy for crystallochemical analyses of complex hydrous silicates: I. Amphiboles. *Am. Mineral.*, **100**, 2682–2694.

Löwenstein, W. (1954): The distribution of aluminum in the tetrahedra of silicates and aluminates. *Am. Mineral.*, **39**, 92–96.

Ma, C., Kampf, A.R., Connolly, H.C, Jr, Beckett, J.R., Rossman, G.R., Sweeney Smith, S.A., Schrader, D.L. (2011): Krotite, $CaAl_2O_4$, a new refractory mineral from the NWA 1934 meteorite. *Am. Mineral.*, **96**, 709–715.

MacMillan, P.F. & Hofmeister, A.M. (1988): Infrared and Raman spectroscopy. *in* "Spectroscopic Methods in Mineralogy and Geochemistry", F.C. Hawthorne, ed. *Rev. Mineral.*, **18**, 99–159.

McMillan, P.F. & Hess, A.C. (1988): Symmetry, group theory and quantum mechanics. *in* "Spectroscopic Methods in Mineralogy and Geochemistry", F.C. Hawthorne, ed. *Rev. Mineral*., **18**, 11–61.

Morimoto, N.M., Fabries, J., Ferguson, A.K., Ginzburg, I.V., Ross, M., Seifert, F.A., Zussman, J. (1989): Nomenclature of pyroxenes. *Mineral. J.*, **14**, 198–221.

Mottana, A., Paris, E., Della Ventura, D., Robert, J.L. (1990): Spectroscopic evidence for tetrahedrally-coordinated titanium in richteritic amphiboles. *Rend. Lincei*, **1**, 387–392.

Neuville, D.R., de Ligny, D., Henderson, G.S. (2014): Advances in Raman Spectroscopy applied to Earth and Material Sciences. *in* "Spectroscopic Methods in Mineralogy and Material Sciences", G.S. Henderson, D.R. Neuville, R.T. Downs, eds. *Rev. Mineral. Geochem*., **78**, 509–541.

Oberti, R., Hawthorne, F.C., Ungaretti, L., Cannillo, E. (1995a): $^{[6]}$Al disorder in amphiboles from mantle peridotites. *Can. Mineral.*, **33**, 867–878.

Oberti, R., Sardone, N., Hawthorne, F.C., Raudsepp, M., Turnock, A.C. (1995b): Synthesis and crystal-structure refinement of synthetic fluor-pargasite. *Can. Mineral.*, **33**, 25–31.

Oberti, R., Hawthorne, F.C., Cámara, F., Raudsepp, M. (1998): Synthetic fluoro-amphiboles: site preferences of Al, Ga, Sc and inductive effects on mean bond-lengths of octahedra. *Can. Mineral.*, **36**, 1245–1252.

Oberti, R., Hawthorne, F.C., Cannillo, E., Cámara, F. (2007): Long-range order in amphiboles. *in* "Amphiboles: Crystal Chemistry, Occurrence and Health Issues", F.C. Hawthorne, R. Oberti, G. Della Ventura, A. Mottana, eds. *Rev. Mineral. Geochem*., **67**, 125–172.

Palke, A.C., Geiger, C.A., Stebbins, J.F. (2015a): An investigation of local; Fe^{2+} order-disorder in a mantle grospydite garnet using paramagnetically shifted ^{27}Al and ^{29}Si MAS NMR resonances. *Eur. J. Mineral.*, **27**, 463–470.

Palke, A.C., Stebbins, J.F., Geiger, C.A., Tippelt, G. (2015b): Cation order-disorder in Fe-bearing pyrope and grossular garnets: A ^{27}Al and ^{29}Si MAS NMR and ^{57}Fe Mössbauer study. *Am. Mineral.*, **100**, 536–547.

Parthasarathy, S., Nishiyama, Y., Ishii, Y. (2013): Sensitivity and resolution enhanced solid-state NMR for paramagnetic systems and biomolecules under very fast magic angle spinning. *Accounts Chem. Res.*, **46**, 2127–2135.

Pauling, L. (1960): The nature of the chemical bond. 3rd ed. Cornell University Press, Ithaca, New York.

Pell, A.J. & Pintacuda, G. (2015): Broadband solid-state MAS NMR of paramagnetic systems. *Prog. Nucl. Mag. Res. Spec.*, **84–85**, 33–72.

Raudsepp, M., Turnock, A.C., Hawthorne, F.C., Sherriff, B.L., Hartman, J.S. (1987): Characterization of synthetic pargasitic amphiboles ($NaCa_2Mg_4M^{3+}Si_6Al_2O_{22}(OH,F)_2$; M^{3+} = Al, Cr, Ga, Sc, In) by infrared spectroscopy, Rietveld structure refinement and ^{27}Al, ^{29}Si, and ^{19}F MAS NMR spectroscopy. *Am. Mineral.*, **72**, 580–593.

Raudsepp, M., Turnock, A.C., Hawthorne, F.C. (1991): Amphiboles synthesis at low-pressure: what grows and what doesn't. *Eur. J. Mineral.*, **3**, 983–1004.

Robert, J.L. & Della Ventura, G. (1989): The infrared OH-stretching region of synthetic richterites in the system Na_2O-K_2O-CaO-MgO-SiO_2-H_2O-HF. *Eur. J. Mineral.*, **1**, 203–212.

Robert, J.-L., Della Ventura, G., Hawthorne, F.C. (1999): Near-infrared study of short-range disorder of OH and F in monoclinic amphiboles. *Am. Mineral.*, **84**, 86–91.

Skogby, H. & Rossman, G.R. (1991): The intensity of amphibole OH bands in the infrared absorption spectrum. *Phys. Chem. Minerals.*, **18**, 64–68.

Skogby, H., Bosi, F., Lazor, P. (2012): Short-range order in tourmaline: a vibrational spectroscopic approach to elbaite. *Phys. Chem. Minerals*, **39**, 811–816.

Stebbins, J.F. (1988): NMR spectroscopy and dynamic processes in mineralogy and geochemistry. *in* "Spectroscopic Methods in Mineralogy and Geochemistry", F.C. Hawthorne, ed. *Rev. Mineral.*, **18**, 405–429.

Stebbins, J.F. & Xue, X. (2014): NMR spectroscopy of inorganic Earth materials. *in* "Spectroscopic Methods in Mineralogy and Material Sciences", G.S. Henderson, D.R. Neuville, R.T. Downs, eds. *Rev. Mineral. Geochem*., **78**, 605–653.

Strens, R.G.J. (1966): Infrared study of cation ordering and clustering in some (Fe,Mg) amphibole solid solutions. *Chem. Comm. (Chem. Soc. London)*, **15**, 519–520.

Tait, K.T., Hawthorne, F.C., Della Ventura, G. (2001): Al-Mg disorder in a gem-quality pargasite from Baffin Island, Nunavut, Canada. *Can. Mineral.*, **9**, 1725–1732.

Taylor, M.C., Cooper, M.A., Hawthorne, F.C. (1995): Local charge-compensation in hydroxyl-deficient uvite. *Can. Mineral.*, **33**, 1215–1221.

Watenphul, A., Burgdorf, M., Schlüter, J., Horn, I., Malcherek, T., Mihailova, B. (2016): Exploring the potential of Raman spectroscopy for crystallochemical analyses of complex hydrous silicates: II. Tourmalines. *Am. Mineral.*, **101**, 970–985.

Wickramasinghe, N.P., Shaibat, M.A., Jones, C.R., Casabianca, L. B., de Dios, A.C., Harwood, J.S., Ishii, Y. (2008): Progress in ^{13}C and ^{1}H solid-state nuclear magnetic resonance for paramagnetic systems under very fast magic angle spinning. *J. Chem. Phys.*, **128**, 052210–1-15.

Received 19 November 2015
Modified version received 19 February 2016
Accepted 4 March 2016